Air–Ice–Ocean Momentum Exchange. Part II: Ice Drift

WILL PERRIE AND YONGCUN HU

Ocean Sciences Division, Fisheries and Oceans Canada, Bedford Institute of Oceanography, Dartmouth, Nova Scotia, Canada

(Manuscript received 18 October 1995, in final form 25 February 1997)

ABSTRACT

A model was constructed to estimate ice floe trajectories. The model considers the balance of atmosphere and ocean drag forces on ice floes, including skin and body drag forces from wind, waves, and currents. Discussion of air–ice and water–ice skin stresses, water–ice form stress, and wave radiation stress is presented. Estimates are presented for the ice drift in a variety of hypothetical situations: (i) as a function of ice floe diameter, thickness, and concentration; (ii) in ''wave'' and ''no wave'' situations; and (iii) in constant wind forcing and time-varying wind forcing situations. The model is shown to be consistent with wave and ice observations collected during the Labrador Ice Margin Experiment 1987 on the Grand Banks during relatively high wind situations. Combining this model with the wave-scattering model of Part I allows estimation of 1) the effect of wave scattering attenuation on ice floe trajectories and the ice edge and 2) the effect of ice floe drift on the wave spectra. Thus, an enhanced modeling of wave and ice dynamics is achieved.

1. Introduction

Part I (Perrie and Hu 1996) considered the relation between wave attenuation λ, MIZ ice floe parameters, wind, and wave conditions. It was suggested that λ depends strongly on wave frequency f, floe diameter L, ice cover concentration fi, and wave age. Ice floe thickness, wind speed U_{10}, wave energy $E(f, \vartheta)$, and spatial position within the marginal ice zone (MIZ) were found to be less important factors. Under appropriate MIZ conditions (regarding fi and L, for example), wave generation and growth occurs. Under other conditions, all energy but that of the very lowest frequency bands is dampened. Throughout Part I, MIZ ice floes were assumed not to drift. The effects of ice drift are considered in this paper. Moreover, we are now concerned with the movement of ice floes in response to wind, waves, and currents. A related concern is the wave spectra in near-MIZ waters, where waves are scattered and attenuated by ice floes, which are allowed to drift in response to wind, waves, and currents.

Interactions between ice, wind, waves, and currents can dramatically move the ice edge. During high wind or storm situations, the ice edge can move as much as 50 km or more in a day, as observed during the Labrador Ice Margin Experiment (McNutt et al. 1988). However, ice edge predictability on the timescale of hours or days is not clearly understood. The ice edge and the distribution of ice floes are moved by wind, waves, and currents. Moreover, compared to the ice-free situation, currents, waves, and the associated planetary boundary layer are altered by the MIZ. Our model for the ice edge and ice floe trajectories is based on a balance equation for forces due to wind, waves, and currents impinging on the ice, following Tang and Fissel (1991), Steele et al. (1989), and Jenkins (1987a,b, 1989).

Ocean surface waves are central to the atmosphere–ocean coupling dynamics at the air–sea interface. The dominating physical processes that determine ocean surface waves are input of energy due to wind S_{in}, nonlinear transfer between spectral components due to wave–wave interactions S_{nl}, and energy dissipation due to white capping and wave breaking S_{ds}. Operational wave models combine these processes in the energy balance equation, which may be written as

$$\frac{\partial E(f, \vartheta)}{\partial t} + \mathbf{C}_g \cdot \nabla E(f, \vartheta) = S_{\text{in}} + S_{\text{ds}} + S_{\text{nl}}, \quad (1)$$

where the two-dimensional wave spectrum $E(f, \vartheta)$ is a function of frequency f, direction ϑ, time t, and position $\mathbf{x}$, and where $\mathbf{C}_g$ is the group velocity. Examples of how S_{in}, S_{nl}, and S_{ds} may be parameterized are presented in Hasselmann et al. (1988) and Perrie et al. (1989).

Section 2 presents a model for ice floe trajectories, hereafter denoted the *drift* model. Ice floe drift involves skin and body drag due to wind, waves, and surface currents. For surface currents, we include Ekman transport and currents arising from the wind-forced wave field, but not background currents from wind-induced sea surface slope or any underlying circulation. Section 3 investigates the characteristics of the drift model, us-

Corresponding author address: Dr. Will Perrie, Ocean Sciences Division, Fisheries and Oceans Canada, Bedford Institute of Oceanography, P.O. Box 1006, Dartmouth NS B2Y 4A2, Canada.
E-mail: wperrie@emerald.bio.dfo.ca

ing a simple square-box SWAMP (Sea Wave Modelling Program) ocean and hypothetical wind fields, as used by The SWAMP Group (1985) in intercomparing wave models. Section 4 presents the results of real data tests for the Labrador Ice Margin Experiment (LIMEX) 1987 program in the northwest Atlantic, as described by McNutt et al. (1988). During high wind conditions, we demonstrate that the drift model generates ice edge estimates that are largely consistent with observations. Moreover, we present a partial verification of a combined scattering–drift model, implementing the *scattering* model from Part I into the *drift* model. The scattering–drift model provides estimates for MIZ ice edge evolution and the wave spectra in near-MIZ open ocean waters.

2. Waves, currents, and ice floe drift

a. Wave-induced surface current

Given wind fields $\mathbf{U}_{10}$ at 10-m reference height, the wave balance equation (1) gives the two-dimensional spectral wave energy $E(f, \vartheta)$. The associated Stokes drift is the mean velocity following a fluid particle and therefore, by definition, is a Lagrangian property. Letting $\mathbf{U}_S$ be the Lagrangian velocity of a particle at initial position $(\mathbf{x}, c, t = 0)$, then the Stokes drift at time t is simply

$$\mathbf{U}_S(\mathbf{x}, t) = 4\pi \int \int f\mathbf{k}e^{2kc}E(f, \vartheta)\, df\, d\vartheta, \qquad (2)$$

following Huang (1971) and Jenkins (1989). The vertical Lagrangian coordinate c corresponds to the usual vertical Eulerian coordinate z at initial time $t = 0$.

Equation (2) is a diagnostic relation for current as a function of depth, whereas Eq. (1) gives the evolution of $E(f, \vartheta)$ in position and time coordinates $(\mathbf{x}, t)$. Following Jenkins (1987a,b, and 1989), the *quasi-Eulerian* current $\mathbf{U}_E$ is given by

$$\frac{\partial \mathbf{U}_E}{\partial t} + \vec{\mathbf{f}} \times \mathbf{U}_E - \frac{\partial}{\partial c}\left(\nu \frac{\partial \mathbf{U}_E}{\partial c}\right) = -\vec{\mathbf{f}} \times \mathbf{U}_S - 2\pi \int df \int d\vartheta f\mathbf{k}S_{ds}2kNe^{2kc}, \qquad (3)$$

where ice floes are *not* assumed present. The quasi-Eulerian current is equal to the Lagrangian-mean current $\mathbf{U}_L$ minus the Stokes drift $\mathbf{U}_S$ and can be thought of as being equal to the Eulerian-mean current $\mathbf{U}_e$, referred to as a Lagrangian coordinate system (Jenkins 1987b). The Eulerian-mean current $\mathbf{U}_e$ is the vector-averaged water particle velocity at a fixed spatial position. As long as particle displacements are not so large as to move from one space grid to another, which is generally true for this study, we may identify the quasi-Eulerian and the Eulerian mean currents: $\mathbf{U}_E = \mathbf{U}_e$. Other variables for Eq. (3) are ν, the eddy viscosity, and $\vec{\mathbf{f}}$, the Coriolis acceleration [$|\vec{\mathbf{f}}| \equiv 2\Omega \sin(\phi)$ where Ω is the earth's angular velocity and ϕ is the latitude]. Unit vector $\mathbf{k} = (\cos(\pi/2 - \vartheta), \sin(\pi/2 - \vartheta))$ is related to wavenumber k by $\vec{\mathrm{k}} = k\mathbf{k}$. The integral expression on the right side of Eq. (3) represents the generation of $\mathbf{U}_E$ from the waves through wave dissipation S_{ds}. The parameterization for S_{ds} follows Hasselmann et al. (1988). Coefficient N represents momentum transfer from waves to current. Because no consensus exists on the form for N, we assume $N = 1$, following Jenkins (1989). Finally, the last term on the left side of Eq. (3),

$$-\frac{\partial}{\partial c}\left(\nu \frac{\partial \mathbf{U}_E}{\partial c}\right),$$

represents the vertical transport of momentum by viscous shear stress.

The boundary condition at the sea surface is

$$\nu \left.\frac{\partial \mathbf{U}_E}{\partial c}\right|_{c=0} = \frac{\boldsymbol{\tau}}{\rho_w} - 2\pi \int df \int d\vartheta f\mathbf{k}S_{in}, \qquad (4)$$

where $\tau \equiv \rho_a U_*^2 = \rho_a C_D |\mathbf{U}_{10}^2|$ is the wind stress on the water surface, ρ_a is the density of air, ρ_w is the density of water, and C_D is the air–water drag coefficient. The wind stress is assumed in the wind direction. The parameterization for S_{in} follows Hasselmann et al. (1988). The integral on the right side of Eq. (4) represents the momentum transfer from wind into the waves. Following Smith (1991) and Smith et al. (1992), the air–water drag coefficient C_D is parameterized as

$$C_D = \begin{cases} C_S + (1.85 - 2.24C_p/(U_{10}\cos[\vartheta - \theta_{10}])) \times 10^{-3}, \\ \qquad \text{when } C_p/U_{10}\cos\vartheta < 0.82 \\ C_S, \quad \text{otherwise,} \end{cases} \qquad (5)$$

where C_S is the open-ocean, long-fetch, drag coefficient proposed by Smith (1988), θ_{10} is the wind direction, $C_p = g/2\pi f_p$ is the phase speed, and f_p is the spectral peak frequency. This C_D parameterization implies that *young* waves can be as much as three times rougher than *old* waves. This is important for modeling the currents associated with young waves.

The profile for eddy viscosity ν is assumed to follow Madsen (1977), Weber (1981), and Jenkins (1987a,b, and 1989), as given in Fig. 1. It has a constant portion in the uppermost 1 cm with a linear variation

$$\nu = -0.4u_*^w c \qquad (6)$$

between 1 cm and 12 m depth, where u_*^w is the water friction velocity. The water friction velocity may be expressed as

$$u_*^w = \sqrt{\frac{\rho_a}{\rho_w}} U_*, \qquad (7)$$

where U_* is the *air* friction velocity. A second linear portion is assumed to extend from 12 m to 50 m depth, as indicated in Fig. 1. As no consideration has been

made for the effects of ice floe draft on eddy viscosity, this model is most valid for low ice cover concentrations.

Equations (2)–(4) are solved using a finite-difference method and implicit time stepping to satisfy stability conditions. A grid of 200 points was used in the depth direction [0, 100] m. The grid size varied from being tiny, 5 mm, at the surface to ~1 m at the bottom. We assume the bottom boundary condition $\mathbf{U}_E = 0$. The time step for the current model was ≈70 sec because of the 5-mm grid spacing just below the water surface and the usual stability criterion. By comparison, the time step and grid spacing were 1200 sec and 50 km for the wave model. The Coriolis parameter $|\vec{\mathbf{f}}|$ was set to 1.07×10^{-4} s^{-1}, corresponding to 50°N latitude.

Because we are concerned with the motion of ice floes in response to wind, waves, and currents rather than the details of wave generation and propagation, we use a simple well-tuned operational wave model to represent the evolution of the wave spectrum $E(f, \vartheta)$. Specifically, we use a second-generation wave model, as described by Resio (1981), Perrie and Toulany (1985), and Perrie et al. (1989). The nonlinear transfer S_{nl} is parameterized in terms of a few spectral wave parameters such as peak frequency f_p, spectra peakedness γ, and the Phillips (1985) α coefficient.

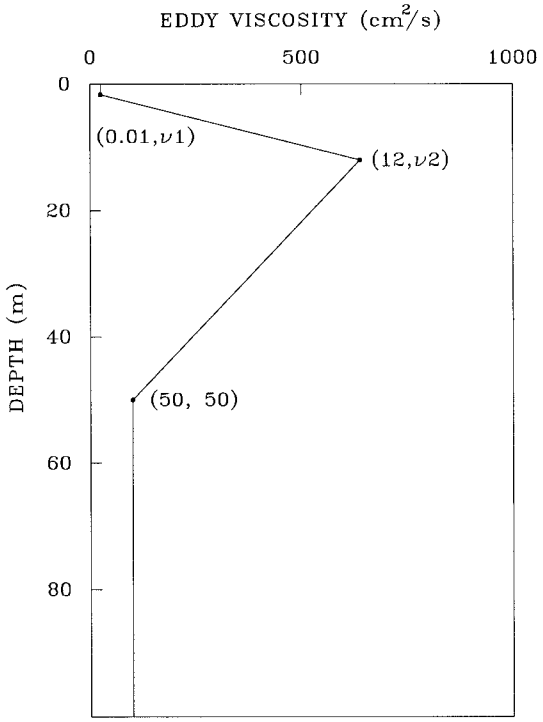

FIG. 1. The assumed profile of eddy viscosity ν as a function of water depth, where $\nu_1 = -0.4u_*^w c|_{c=0.01}$, $\nu_2 = -0.4u_*^w c|_{c=12.0}$, and u_*^w is the water friction velocity.

b. Ice floe drift

Following Tang and Fissel (1991) and Steele et al. (1989), the equation of motion for an ice floe in response to wind, waves, and currents is

$$m\frac{\partial \mathbf{u}'}{\partial t} + m\vec{\mathbf{f}} \times \mathbf{u}' = A(\boldsymbol{\tau}_{\text{air}}^{\text{skin}} + \boldsymbol{\tau}_{\text{water}}^{\text{skin}} + \boldsymbol{\tau}_{\text{air}}^{\text{form}} + \boldsymbol{\tau}_{\text{water}}^{\text{form}} + \boldsymbol{\tau}_{\text{rad}}^{\text{wave}}) - mg\boldsymbol{\nabla}\xi + \mathbf{F}, \quad (8)$$

where g is the acceleration due to gravity, m is the ice mass, A is the ice floe surface area, ξ is the sea surface elevation, $\mathbf{F}$ is the ice internal stress gradient, $\mathbf{u}'$ is the *absolute* ice velocity, $\boldsymbol{\tau}_{\text{air}}^{\text{skin}}$ is the wind stress on the top surface of the ice floe, $\boldsymbol{\tau}_{\text{water}}^{\text{skin}}$ is the water stress on the bottom surface of the ice floe, $\boldsymbol{\tau}_{\text{air}}^{\text{form}}$ is the air–ice form stress, $\boldsymbol{\tau}_{\text{water}}^{\text{form}}$ is the water–ice form stress, and $\boldsymbol{\tau}_{\text{rad}}^{\text{wave}}$ is the wave radiation pressure. We neglect nonlinear advection, following Jenkins (1987a,b, 1989), Tang and Fissel (1991), and Steele et al. (1989), in order to maintain computational efficiency in the model.

If the ice concentration is low, the internal stress gradient $\mathbf{F}$ is essentially zero. Replacing $-mg\boldsymbol{\nabla}\xi$ by the geostropic current $m\vec{\mathbf{f}} \times \mathbf{U}_g$ and neglecting $\mathbf{F}$, we express Eq. (8) as

$$\frac{\partial \mathbf{u}}{\partial t} + m\mathbf{f} \times \mathbf{u} = A(\boldsymbol{\tau}_{\text{air}}^{\text{skin}} + \boldsymbol{\tau}_{\text{water}}^{\text{skin}} + \boldsymbol{\tau}_{\text{air}}^{\text{form}} + \boldsymbol{\tau}_{\text{water}}^{\text{form}} + \boldsymbol{\tau}_{\text{rad}}^{\text{wave}}), \quad (9)$$

which gives the ice floe velocity, $\mathbf{u} = \mathbf{u}' - \mathbf{U}_g$, relative to the geostropic current $\mathbf{U}_g$. Section 3 presents computations of $\mathbf{u}$ for hypothetical wind situations. Because $\mathbf{u}'$ and $\mathbf{U}_g$ always occur in the combination $\mathbf{u}' - \mathbf{U}_g$, the $\mathbf{u}$ computations in section 3 are identical to those for $\mathbf{u}'$, calculated with $\mathbf{U}_g = 0$.

The stresses $\boldsymbol{\tau}_{\text{air}}^{\text{skin}}$ and $\boldsymbol{\tau}_{\text{water}}^{\text{skin}}$ are caused by skin friction. Steele et al. (1989) suggest that form drag may be actually greater, or of the same order, as skin friction drag for small thick floes at low ice cover concentrations. This includes many commonly occurring MIZ situations. However, since the freeboard of a typical ice floe is about one-tenth of its draft and the atmospheric boundary layer depth is about 10 times that of the ocean, it follows that $|\boldsymbol{\tau}_{\text{air}}^{\text{form}}| \ll |\boldsymbol{\tau}_{\text{water}}^{\text{form}}|$. Moreover, Steele et al. (1989) suggest that $\boldsymbol{\tau}_{\text{air}}^{\text{form}}$ is implicitly included in field measurements of $\boldsymbol{\tau}_{\text{air}}^{\text{skin}}$. Therefore, the final time-dependent equation of motion for an ice floe becomes

$$\frac{\partial \mathbf{u}}{\partial t} + \vec{\mathbf{f}} \times \mathbf{u} = \frac{A}{m}(\boldsymbol{\tau}_{\text{air}}^{\text{skin}} + \boldsymbol{\tau}_{\text{water}}^{\text{skin}} + \boldsymbol{\tau}_{\text{water}}^{\text{form}} + \boldsymbol{\tau}_{\text{rad}}^{\text{wave}}). \quad (10)$$

To solve this equation, we need to know $\boldsymbol{\tau}_{\text{air}}^{\text{skin}}$, $\boldsymbol{\tau}_{\text{water}}^{\text{skin}}$, $\boldsymbol{\tau}_{\text{water}}^{\text{form}}$, and $\boldsymbol{\tau}_{\text{rad}}^{\text{wave}}$. These are nonlinear functions of the ice velocity $\mathbf{u}$.

The air–ice skin friction stress $\boldsymbol{\tau}_{\text{air}}^{\text{skin}}$ is usually represented by a quadratic formula in terms of the wind $\mathbf{U}_{10}$:

$$\boldsymbol{\tau}_{\text{air}}^{\text{skin}} \equiv \rho_a C_{ai}^s |\mathbf{U}_{10} - \mathbf{u}|(\mathbf{U}_{10} - \mathbf{u}), \quad (11)$$

where ρ_a is the air density and C_{ai}^{s} is the air–ice skin

friction drag coefficient. Tang and Fissel (1991) suggest that $C^s_{ai} \approx 1\text{–}5 \times 10^{-3}$. We used $C^s_{ai} \approx 3 \times 10^{-3}$, following Steele et al. (1989).

Analogous to Eq. (11), the water–ice skin friction stress $\boldsymbol{\tau}^{skin}_{water}$ may be represented as

$$\boldsymbol{\tau}^{skin}_{water} \equiv -\rho_w C^s_{wi} |\mathbf{u} - \mathbf{U}_e| (\mathbf{u} - \mathbf{U}_e), \quad (12)$$

where ρ_w is the water density, C^s_{wi} is the water–ice skin friction drag coefficient, and $\mathbf{U}_e$ is the Eulerian current at the z grid point just below $z = -D$, where D is the ice draft. Tang and Fissel (1991) suggest that $C^s_{wi} \approx 15\text{–}25 \times 10^{-3}$. We used $C^s_{wi} \approx 2 \times 10^{-2}$. An approximation is being made here. There is a turbulent boundary layer beneath the ice, which responds to the wind and is directly associated with wind waves. Since the detailed structure of the boundary layer is not of interest, the water–ice skin friction drag is expressed by the familiar quadratic law with a drag coefficient. The water velocity $\mathbf{U}_e$ in Eq. (12) should be the ocean current at the base of the turbulent boundary layer. However, we do not know the depth of the turbulent boundary layer. If we assume that it is quite thin, then it is a good approximation to use the water velocity at the ocean grid point, which lies just below the ice draft, $-D$. Properties of the related boundary layer under waves have been considered by Yoshikawa et al. (1988), Toba and Kawamura (1996), and Thorpe (1986, 1992).

The water–ice form stress $\boldsymbol{\tau}^{form}_{water}$ describes the normal force acting on the leading face of an ice floe as it moves through the water at relative velocity $\mathbf{u} - \bar{\mathbf{U}}_e$. Following Steele et al. (1989), the general form for $\boldsymbol{\tau}^{form}_{water}$ is

$$\boldsymbol{\tau}^{form}_{water} = -\frac{2}{\pi}\rho_w C^f_{wi}\frac{D}{L}|\mathbf{u} - \bar{\mathbf{U}}_e|(\mathbf{u} - \bar{\mathbf{U}}_e)\Gamma, \quad (13)$$

where C^f_{wi} is the water–ice form drag coefficient, L is the ice floe diameter, DL is the ice floe cross section, and $\bar{\mathbf{U}}_e$ is the Eulerian current, vertically averaged over the leading face of the floe

$$\bar{\mathbf{U}}_e = \frac{1}{D}\int_{-D}^{0} \mathbf{U}_e(z)\, dz. \quad (14)$$

Hoerner (1965) and Steele et al. (1989) suggest the approximation $C^f_{wi} \approx 1$, which is valid for a wide range of Reynolds numbers. The parameter Γ describes the reduction in drag due to the wake effect

$$\Gamma = \left(1 - \sqrt{\frac{D}{L_f}}\right)^2, \quad (15)$$

where L_f is the effective average fetch between ice floes. Using the parameterization for L_f from Steele et al. (1989), then for circular ice floes, $L_f = L/2\sqrt{\pi([1/\text{fi}] - 1)}$.

The wave radiation pressure $\boldsymbol{\tau}^{wave}_{rad}$ represents the force exerted on ice floes by reflected and diffracted waves. Following Wadhams (1983) and Steele et al. (1989), the force on a floe of diameter L, due to perfect reflection of surface waves, is

$$F_{rad} = \frac{1}{2}\rho_w g a^2 L, \quad (16)$$

where a is the wave amplitude. In terms of the effective average fetch between ice floes, L_f, the standard fetch relations for growing waves, as suggested by Hasselmann et al. (1973), Steele et al. (1989), and Perrie and Toulany (1990) then imply

$$a^2 = 3.2 \times 10^{-4}\left(\frac{\tau}{\rho_a}\right)\left(\frac{L_f}{g}\right), \quad (17)$$

where τ is the air–water stress. Using the parameterization for L_f for circular ice floes,

$$L_f = \frac{L}{2}\sqrt{\pi\left(\frac{1}{\text{fi}} - 1\right)},$$

as given above, it follows that

$$\boldsymbol{\tau}^{wave}_{rad} = 3.2 \times 10^{-4}\frac{\rho_w}{\rho_a}\sqrt{\frac{1}{\pi}\left(\frac{1}{\text{fi}} - 1\right)}\boldsymbol{\tau}, \quad (18)$$

where fi is the ice cover concentration. Thus, $\boldsymbol{\tau}^{wave}_{rad}$ depends on wind stress $\tau = \rho_a C_D U^2_{10}$ and ice cover concentration.

The wave radiation parameterization described here is necessary. Although we use a discrete spectral wave model, as described in section 2a, model implementations involve spatial grids of 50 km for the simple square-box SWAMP ocean. For the real ocean, the wave model grid is 1.5°, or about 136 km. Therefore, the resolution of spatial grids used in our wave model implementations is very coarse, compared to the spacing between MIZ ice floes. For example, for floes 50 m in diameter at 10% coverage, the effective distance between floes is about 0.5 km, which is much smaller than the resolution of our finest possible grid.

Equation (10) is our basic governing equation for ice floe drift in section 3. The stresses we consider, $\boldsymbol{\tau}^{skin}_{air}$, $\boldsymbol{\tau}^{skin}_{water}$, $\boldsymbol{\tau}^{form}_{water}$, and $\boldsymbol{\tau}^{wave}_{rad}$ are given by Eqs. (11)–(18). Other effects, such as the effects due to stratification, are not considered. We calculate wave-induced surface current from wind stress as if no ice were present, following section 2a.

3. Hypothetic wind situations

To understand the basic characteristics of ice floe drift, in response to wind, waves, and currents as represented by the *drift* model, the model was implemented for a simple square-box SWAMP ocean, following The SWAMP Group (1985). Specifically, we assume an infinitely deep ocean consisting of grid points spaced 50 km apart on the X–Y plane, with wind in the positive X-axis direction, as shown in Fig. 2. We consider the dependency of floe velocity on factors such as the presence of waves, floe thickness, floe diameter, and wind speed. For small, thick floes on the order of tens of meters

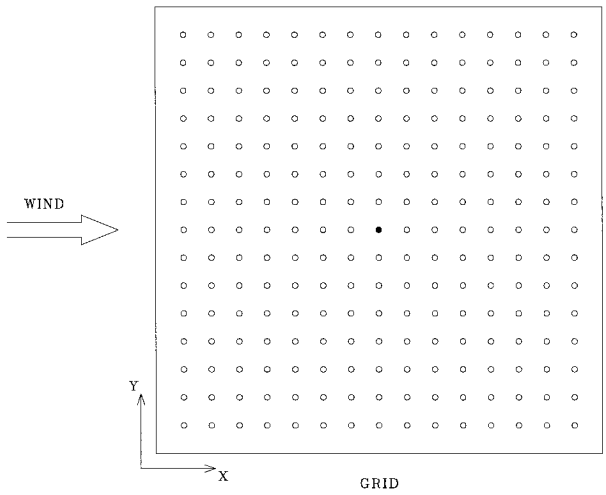

FIG. 2. Grid for the SWAMP square box ocean of The SWAMP Group (1985). Grid points are spaced at 50 km with wind in the positive *X*-axis direction. The ice floe at coordinates (400, 400) is denoted ●.

in diameter, Steele et al. (1989) showed that the wake effect gives a reduction to C^f_{wi} at high ice cover concentrations. This is also considered. Clearly, there are many other factors that could be considered. Part I showed that wave attenuation λ should depend on ice cover concentration fi, ice edge geometry, ice floe diameter, and the distribution of ice floe diameters within the MIZ. It is plausible to expect that these and other factors may also be important for estimation of C^s_{ai}, C^s_{wi}, and C^f_{wi}, (the air–ice and water–ice skin friction drag coefficients, and the water–ice form drag coefficient, respectively).

a. Dependency of floe velocity on waves

The (*X*, *Y*) components of Eulerian current $\mathbf{U}_e(z)$, associated with $\mathbf{U}_E(z)$ in Eqs. (2)–(4), are given in Fig. 3a as a function of depth. This is for coordinates (400, 400) km in Fig. 2. Because the wind is switched on from zero, the circles in *U* and *V* arise from inertial gyres. Net values for *U* and *V* near the surface largely arise from Ekman drift directed to the right of the wind stress. Components of the ice floe velocity **u** are also shown, as given by Eq. (10). The wind speed U_{10} is 10 m s^{-1}. The ice floe is assumed cylindrical in shape, with diameter 10 m and thickness 1 m. Results presented in Fig. 3a start at the origin and extend over a period of 50 h, which exceeds the time needed for the waves to equilibrate. Figure 3a shows that the surface current is about 3% of the wind speed, which is similar to the Lake Huron observations reported by Churchill and Csanady (1983) and the analysis of Jenkins (1987a,b). Estimates for $\mathbf{U}_e(z)$ components, when waves are assumed absent, are also presented. This is achieved by setting $E(f, \vartheta) = 0$, $S_{ds} = 0$, and $S_{in} = 0$ in Eqs. (2)–(4). This shows that waves enhance the surface current in the wind direction, particularly during the first few hours of onset of the wind. With the fresh onset of wind, waves are ''young'' and the drag coefficient C_D is *rough*, as given by Eq. (5).

The effect of wave age dependency on C_D in Eq. (5) is evident from the phase speed relation $C_p = \omega_p/k_p$, where ω_p and k_p are the angular frequency and wavenumber of the spectral peak. From the deep water dispersion relation $\omega_p^2 = gk_p$, wave age may be expressed as $C_p/U_{10} = g/(\omega_p U_{10})$. For a given wind forcing, young waves have a relatively high ω_p. As waves mature and get older, ω_p decreases in magnitude and the wave age $C_p/U_{10} = g/(\omega_p U_{10})$ increases in magnitude. Thus, as waves become more mature, C_D decreases.

Ice floe displacements, corresponding to Fig. 3a, are given in Fig. 3b. The displacements are presented for ''wave'' and ''no wave'' situations as a function of time, with 20-h intervals represented by symbols as indicated. The three panels of Fig. 3b represent

(i) Constant wind $U_{10} = 10$ m s^{-1}

(ii) Alternating wind speeds to simulate rough wave conditions during a storm

$$0 \text{ h} < T \le 6 \text{ h}: \quad U_{10} = 15 \text{ m s}^{-1}$$
$$6 \text{ h} < T \le 12 \text{ h}: \quad U_{10} = 5 \text{ m s}^{-1}$$
$$12 \text{ h} < T \le 18 \text{ h}: \quad U_{10} = 15 \text{ m s}^{-1}$$
$$\ldots \qquad \ldots$$

(iii) A gentle, linearly increasing wind speed,

$$0 \text{ h} < T \le 10 \text{ h}: \quad U_{10} = 6 \text{ m s}^{-1}$$
$$10 \text{ h} < T \le 20 \text{ h}: \quad U_{10} = 7 \text{ m s}^{-1}$$
$$20 \text{ h} < T \le 30 \text{ h}: \quad U_{10} = 8 \text{ m s}^{-1}$$
$$\ldots \qquad \ldots$$
$$90 \text{ h} < T \le 100 \text{ h}: \quad U_{10} = 15 \text{ m s}^{-1},$$

respectively. The second and third panels of Fig. 3b activate young rough waves through a time-varying U_{10} and the HEXOS drag coefficient of Eq. (5). Alternating the wind speed between 5 and 15 m s^{-1} on a 6-hourly basis is a hypothetical test to look at model estimates for surface currents induced by wind and waves in storm situations where wind changes rapidly. Such conditions were encountered during the CASP (the Canadian Atlantic Storm Program, Perrie and Toulany 1990). Thus, we consider an enhanced C_D in association with changing wave regimes: new waves mixing with old waves. This has impact on surface currents through Eq. (3). All results assume a *cold start*, whereby waves, currents, and ice velocities are initially zero.

In each wave case in Fig. 3b, ice floe drift is about ~30% larger than the associated no-wave case. Ice floe drift is therefore enhanced by the effect of waves. The largest enhancement results from rough seas, as modeled by the alternating wind in Fig. 3b (second panel). Alternating wind fields more rapidly, for example every

hour, gives similar results. Part of the effect shown here involves wave radiation pressure $\boldsymbol{\tau}_{\text{rad}}^{\text{wave}}$, which is important for small, thick ice floes, in low concentration situations, as shown in the next section.

b. Floe velocity as a function of floe parameters and wind

In Fig. 3a, the ice floe speed is estimated to be slightly less than that of the surface current, reflecting the balance of wind, waves, and currents in Eq. (10). From Eqs. (11)–(18), the ice floe drift speed **u** should depend on (i) wind speed U_{10}, (ii) current $\mathbf{U}_e$, (iii) ice thickness D, (iv) length of the ice floe L, where length is understood as the dimension in the direction of the wind, and (v) ice cover concentration.

Estimates of the ice floe velocity **u** components as a function of floe thickness are given in Fig. 4a. Assumed values for ice thickness are 0.2, 0.4, and 0.8 m. Although the surface current is the same as that of Fig. 3a, the ice floe velocity is reduced by as much as ~30% for floes 0.8 m thick. The reduction in ice floe speed, with increasing floe thickness D, reflects increasing water–ice form stress $\boldsymbol{\tau}_{\text{water}}^{\text{form}}$, relative to the air–ice skin friction $\boldsymbol{\tau}_{\text{air}}^{\text{skin}}$, despite a slight decrease in water–ice skin friction stress $\boldsymbol{\tau}_{\text{water}}^{\text{skin}}$. As described in Eqs. (11)–(13), $\boldsymbol{\tau}_{\text{air}}^{\text{skin}}$ works to accelerate the ice floe, while $\boldsymbol{\tau}_{\text{water}}^{\text{form}}$ and $\boldsymbol{\tau}_{\text{water}}^{\text{skin}}$ decelerate the floe. The increase in $\boldsymbol{\tau}_{\text{water}}^{\text{form}}$ reflects the thickness D dependence in Eq. (13). Increased D corresponds to reduced currents with increasing depth, which gives the reduction in $\boldsymbol{\tau}_{\text{water}}^{\text{skin}}$.

Estimates of the floe velocity **u** components as a function of ice floe diameter are presented in Fig. 4b. This shows that as ice floes grow in diameter, the drift speed increases. This reflects a reduction in $\boldsymbol{\tau}_{\text{water}}^{\text{form}}$ with increasing floe diameter L, as shown by Eq. (13). The $\boldsymbol{\tau}_{\text{water}}^{\text{form}}$ reduction more than balances increases in $\boldsymbol{\tau}_{\text{water}}^{\text{skin}}$ due to increased $|\mathbf{u} - \mathbf{U}_e|$, where the water velocity $\mathbf{U}_e$ is the current at the ocean grid point which lies just below the ice draft, $-D$.

A composite representation of Figs. 4a–b is given in Fig. 4c, for both wave and no-wave conditions. Here, we simultaneously increase floe diameter and decrease floe draft, keeping the ice floe mass constant. As draft increases and diameter decreases, floe velocity decreases, as in Figs. 4a–b. Analogous results are obtained when waves are absent, although velocity magnitudes are reduced by ~¼, as shown. Figure 4d gives the ice floe stresses and floe speed for ice thickness 0.2, 1, and 5 m as a function of floe diameter. For a given floe diameter, as ice draft increases, $\boldsymbol{\tau}_{\text{water}}^{\text{form}}$ increases, $\boldsymbol{\tau}_{\text{water}}^{\text{skin}}$ decreases, and ice speed decreases, as in Fig. 4a. For a given floe thickness, as floe diameter increases, $\boldsymbol{\tau}_{\text{water}}^{\text{form}}$ decreases, $\boldsymbol{\tau}_{\text{water}}^{\text{skin}}$ increases, and ice speed increases, as in Fig. 4b.

Figure 5a relates mean floe velocity to floe diameter for floes 2 m thick with diameters up to 1000 m. Floe speed can vary from ~2.0% of the wind speed for small diameter floes to ~2.5% of the wind speed for large diameter floes. These results are qualitatively consistent with Steele et al. (1989), showing a 25% speed up for large floes. Corresponding estimates for ice floe stresses are given in Fig. 5b as a function of floe diameter. Whereas water–ice skin friction $\boldsymbol{\tau}_{\text{water}}^{\text{skin}}$ increases with increasing floe diameter, water–ice form drag $\boldsymbol{\tau}_{\text{water}}^{\text{form}}$ decreases. Steele et al. (1989) assume similar values for C_{ai}^{s}, C_{wi}^{s}, and C_{wi}^{f} and report slightly higher floe speeds. Waves are not *explicitly* present in their ocean model and associated ice motion equation.

Because the principal stress accelerating ice floes is $\boldsymbol{\tau}_{\text{air}}^{\text{skin}}$, which has a quadratic dependence on U_{10}, as shown in Eq. (11), we expect that the *fractional* floe velocity, expressed as $\mathbf{u}/U_{10}$, should have an almost linear dependence on U_{10}. This dependence is presented in Fig. 5c, as estimated from the model. Mean floe speed varies from ~2.3% of U_{10}, when $U_{10} = 10$ m s^{-1}, to ~4% of U_{10} when $U_{10} = 18$ m s^{-1}.

Overall model estimates for ice floe velocity as a function of ice draft and diameter are given in Fig. 6a. For a given ice floe diameter, increasing floe draft corresponds to decreasing floe velocity, as also seen in Fig. 4a. For thin floes (<2 m) floe velocity increases slightly with increasing ice diameter, as in Fig. 4b. Thick floes (≥2 m) experience decreasing floe velocity with increasing floe diameter for small diameter floes (<15 m) and increasing velocity with increasing diameter thereafter. Ice floe velocity contours in the no-wave case are similar to contours in the waves case, although 20%–30% smaller in magnitude.

Ice floe stresses and ice floe velocity are given in Fig. 6b, for 50% ice concentration cover and ice drafts 0.2 and 2 m, as a function of floe diameter. For a given floe diameter, as draft increases, $\boldsymbol{\tau}_{\text{water}}^{\text{form}}$ increases, $\boldsymbol{\tau}_{\text{water}}^{\text{skin}}$ decreases, and ice speed decreases, as in Figs. 4a and 6a. For a given floe thickness, as floe diameter increases, $\boldsymbol{\tau}_{\text{water}}^{\text{form}}$ decreases, $\boldsymbol{\tau}_{\text{water}}^{\text{skin}}$ increases, and ice speed increases, as in Figs. 4b and 6a. The decrease in $\boldsymbol{\tau}_{\text{water}}^{\text{form}}$ due to wake effects for small thick floes is also evident. This accounts for the increase in floe velocity with decreasing floe diameter, for thick floes in Fig. 6a.

The variation of floe speed with ice cover concentration and floe diameter is given in Fig. 6c. For moderate (20–60 m) floes, ice speed varies slowly with concentration, whereas for small floes, (~5 m), ice speed increases rapidly with concentration. When concentration is low (<50%), floe speed *largely* increases with increasing floe diameter. When concentration is high (>50%), floe speed decreases with increasing floe diameter; when floe diameter is small (<20 m), the speed increases with increasing floe diameter. This is due to the wake effect as in Fig. 6a. Floe speeds in the waves case are similar to the no-waves case, although smaller in magnitude, as in Fig. 6a.

The variation of ice floe stresses with concentration is given in Fig. 6d. For very small (~5 m) diameter

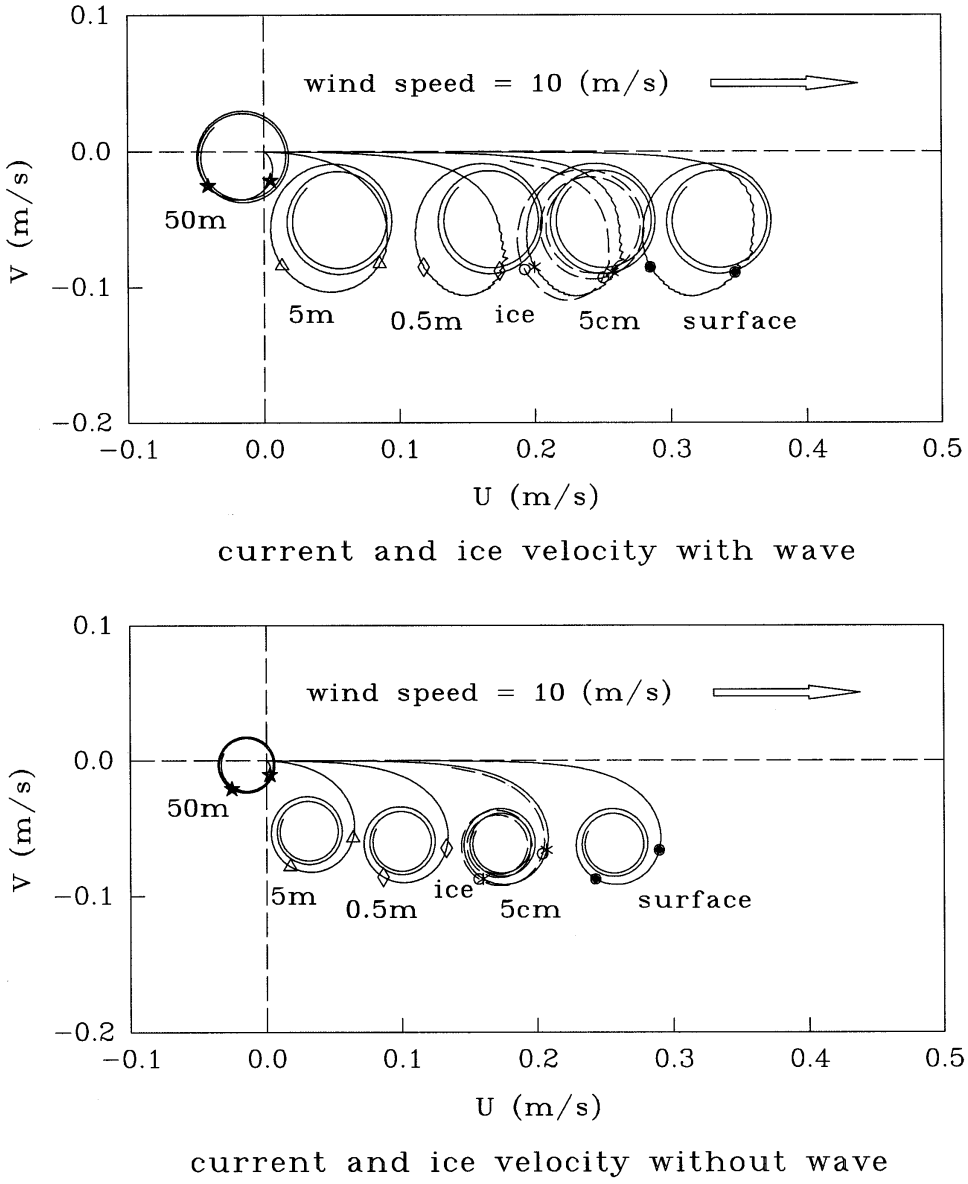

FIG. 3a. Development in time (0 to 50 pendulum hours) of the components of Eulerian velocity $\mathbf{U}_e$, as a function of depth from the ocean surface to a depth 50 m, for (400, 400) in Fig. 2. The ice floe velocity **u** is indicated. The ice floe thickness is 1 m, diameter is 10 m, and wind speed U_{10} is 10 m s^{-1}. At the beginning of the simulation, we set $U = V = 0$. The first symbol ●, ○, *, ◇, △, and ⋆ indicates 5 h, the second indicates 10 h. Both wave and no-wave conditions are presented.

floes, floe speed increases with concentration, whereas for larger (~30 m) floes, floe speed is approximately invariant with respect to concentration, as in Fig. 6c. For ~5 m floes, as concentration decreases, $\boldsymbol{\tau}^{\text{skin}}_{\text{water}}$ decreases. In this situation, while $\boldsymbol{\tau}^{\text{wave}}_{\text{rad}}$ increases, $\boldsymbol{\tau}^{\text{form}}_{\text{water}}$ increases more rapidly and floe speed decreases, corresponding to the wake effect in Fig. 6c. The increase in $\boldsymbol{\tau}^{\text{wave}}_{\text{rad}}$ follows the formulation in Eq. (18). Although $\boldsymbol{\tau}^{\text{wave}}_{\text{rad}}$ works to accelerate the ice floe, it is more than balanced by $\boldsymbol{\tau}^{\text{skin}}_{\text{water}}$ and the rapid increase in $\boldsymbol{\tau}^{\text{form}}_{\text{water}}$. For ~ 30 m floes, as concentration decreases, $\boldsymbol{\tau}^{\text{skin}}_{\text{water}}$ remains almost constant, whereas $\boldsymbol{\tau}^{\text{wave}}_{\text{rad}}$ and $\boldsymbol{\tau}^{\text{form}}_{\text{water}}$ slowly increase. Resultant floe speed is almost constant.

4. LIMEX 1987—The ice edge

a. Overview of the experiment

The Labrador Ice Margin Experiment occurred during 12–19 March 1987. It was part of a comprehensive modeling and field effort by researchers from Canada, the United States, and Europe, and it coincided with

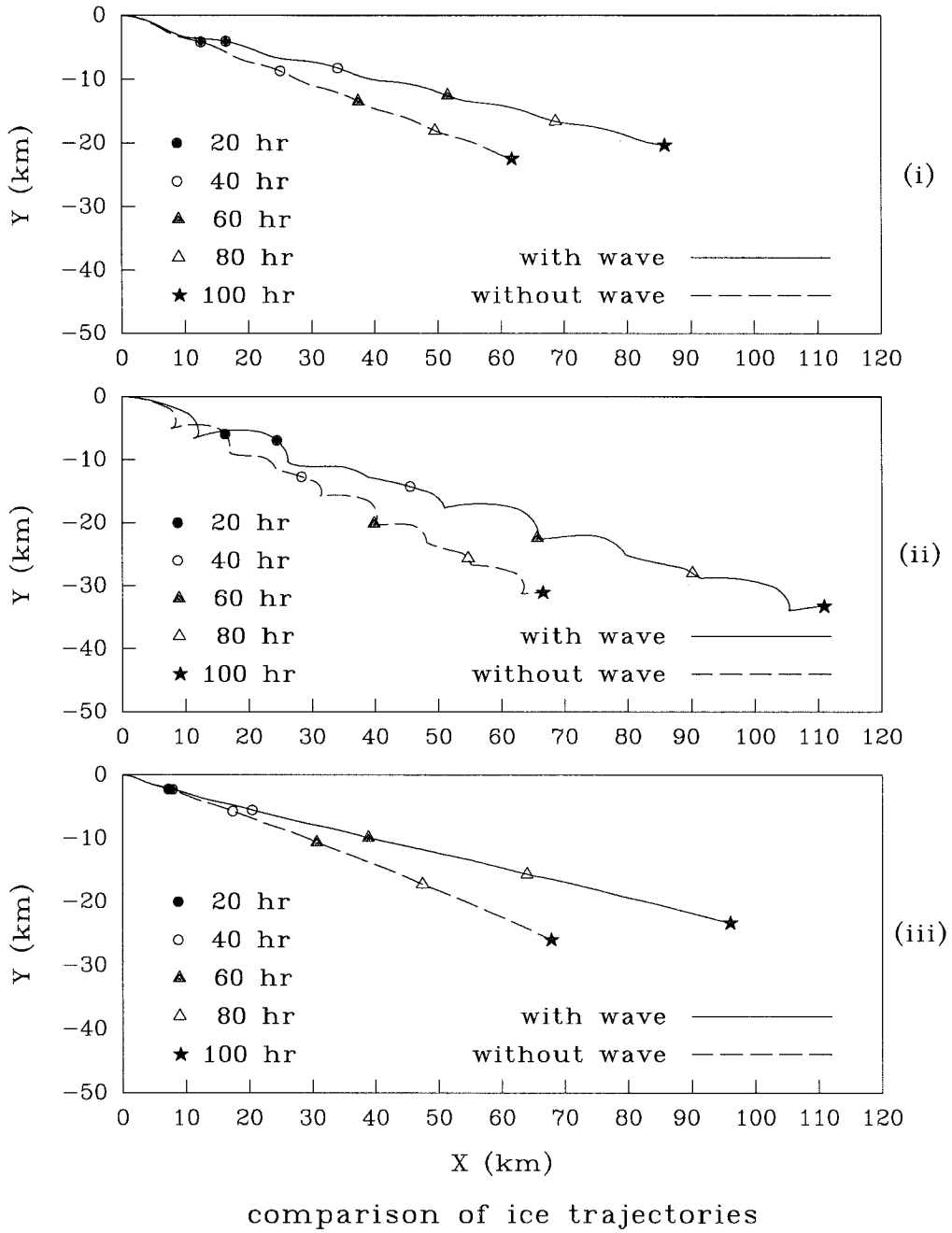

FIG. 3b. As in Fig. 3a comparing accumulated displacements for ice floes in the wave and no-wave cases, at time $t = 0, 20, 40, \cdots, 100$ h, with U_{10} (i) constant 10 m s^{-1}, (ii) alternating between 5 and 15 m s^{-1}, and (iii) increasing gradually from 6 to 15 m s^{-1}.

an international wave experiment known as the Labrador Extreme Wave Experiment (LEWEX). An overview of LEWEX is given by Beal (1991). Our interest in LIMEX/LEWEX is in the observations of the ice edge and wave parameters. Wind fields for the experiment were the result of a careful kinematic analysis, Cardone (1991). Figure 7a shows the wind fields on 14 March near the peak of the main storm event, which occurred at the beginning of LIMEX. Wave spectra were measured by two directional wave buoys, monitored by the Canadian Vessel (CFAV) *Quest* and the Dutch Vessel (HNLMS) *Tydeman*. The positions of these sites are denoted Q and T in Fig. 7a. Modeled and observed wind speed and direction at the *Tydeman* during 9–19 March are given in Figs. 7b–c. The agreement is reasonably good, but not perfect. Although

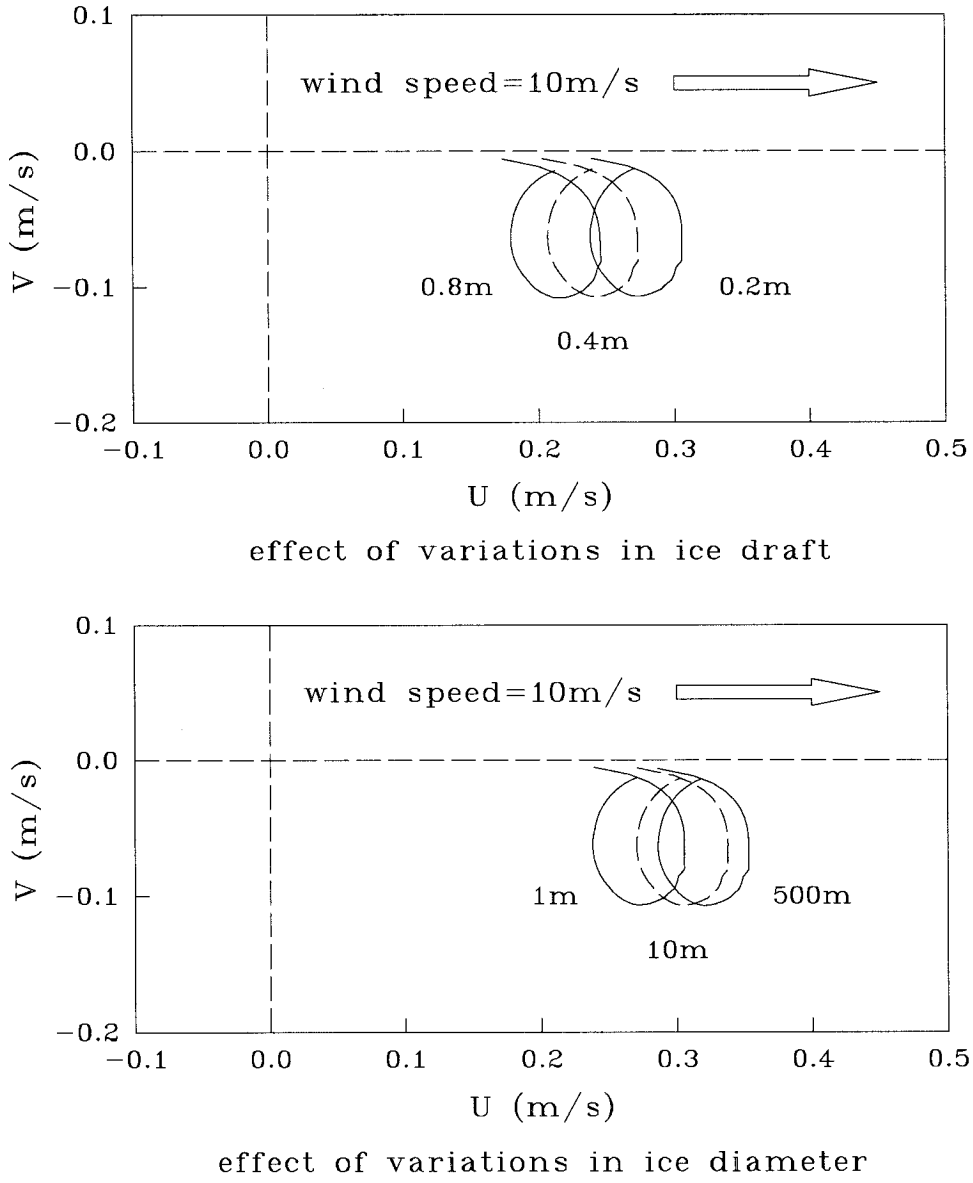

FIG. 4. (a: top) Ice floe velocity components presented as a function of time and ice thickness, as in Fig. 3a. The simulation period is 15 h. The ice floes are 0.2, 0.4, and 0.8 m thick and 1 m in diameter. (b: bottom) Ice floe velocity components, as in (a), but for floe diameters 1, 10, and 500 m and floe thickness 0.2 m.

winds in excess of 15 m s^{-1} did occur on 14 March, much of the experiment involved winds that were $\leq$10 m s^{-1}, particularly during 16–19 March.

At any time during LIMEX, the MIZ was a myriad of distributions, concentrations, thicknesses, and ice floe length scales. Actual values for air–ice and water–ice skin friction stresses, $\boldsymbol{\tau}_{\text{air}}^{\text{skin}}$ and $\boldsymbol{\tau}_{\text{water}}^{\text{skin}}$, water–ice form stress $\boldsymbol{\tau}_{\text{water}}^{\text{form}}$, and wave radiation stress $\boldsymbol{\tau}_{\text{rad}}^{\text{wave}}$ are also highly variable. A detailed modeling of all ice floes with their internal interactions and external coupling mechanisms to winds, currents, and waves goes beyond this paper. Our primary intent is merely to model the ice edge using the drift model in hypothetical and real ocean situations.

b. Model estimates for the ice edge

A definition of the ice edge is somewhat difficult. Ice cover within the MIZ varies widely. Often a distinct ice edge, separating the ice field from open water, does not exist. Following the usual approach, we therefore define the ice edge to be the 10% ice cover contour within the MIZ. Figure 8 presents this ice edge, as observed on 11, 15, and 18 March. During this period, the main ice

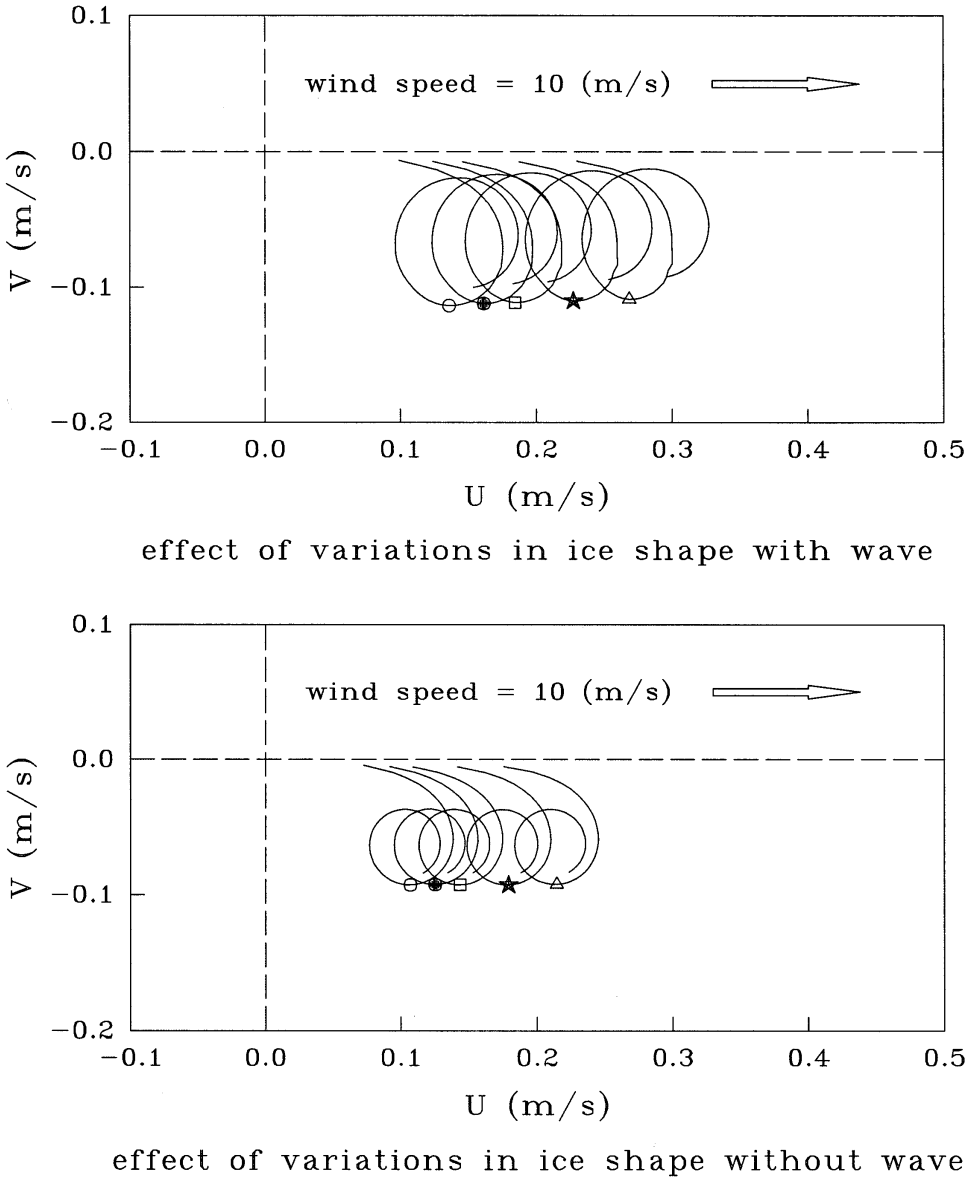

FIG. 4 (*Continued*). (c) Ice floe velocity components, as in (a) but for variations in both floe diameter and floe draft, keeping the ice floe mass constant, assuming waves (upper panel) and no waves (lower panel). Ice floe drafts and diameters of (5, 6.325), (3, 8.165), (2, 10.000), (1, 14.142), and (0.5, 20.000) m are denoted ○, ●, □, ⋆, and △, respectively.

movement is the migration of the ice edge westward. The westward movement is as much as 150 km in the southern part of the ice field. In the northern portion of the ice field, the ice edge sometimes moves eastward.

In estimating the position of the ice edge, we assume that the movement of the 10% ice cover contour matches the movement of individual ice floes. This is an approximation. Convergence/divergence of the ice field may alter the percentage ice cover contours, and therefore the 10% contour may not correspond to the trajectory of specific ice floes. However, in practical terms, this is all the data we have from ice charts during LEWEX/LIMEX. There were no large-scale observations for ice floe trajectories. Therefore, we assume that 10% contour approximates the trajectories of ice floes initially on the 10% line. A plausible argument for this assumption is found in Fig. 6c, showing that for ice floes with moderate diameter (20–60 m), which commonly occur at the MIZ edge, floe speed is approximately independent of ice cover concentration. Regarding ice floe trajectories, this implies that (i) given floes initially ($t = 0$) on the 10% contour, (ii) although these floes may become part of *other* ice cover contours, for example 20% or 30%, as time passes, ($t > 0$), and as

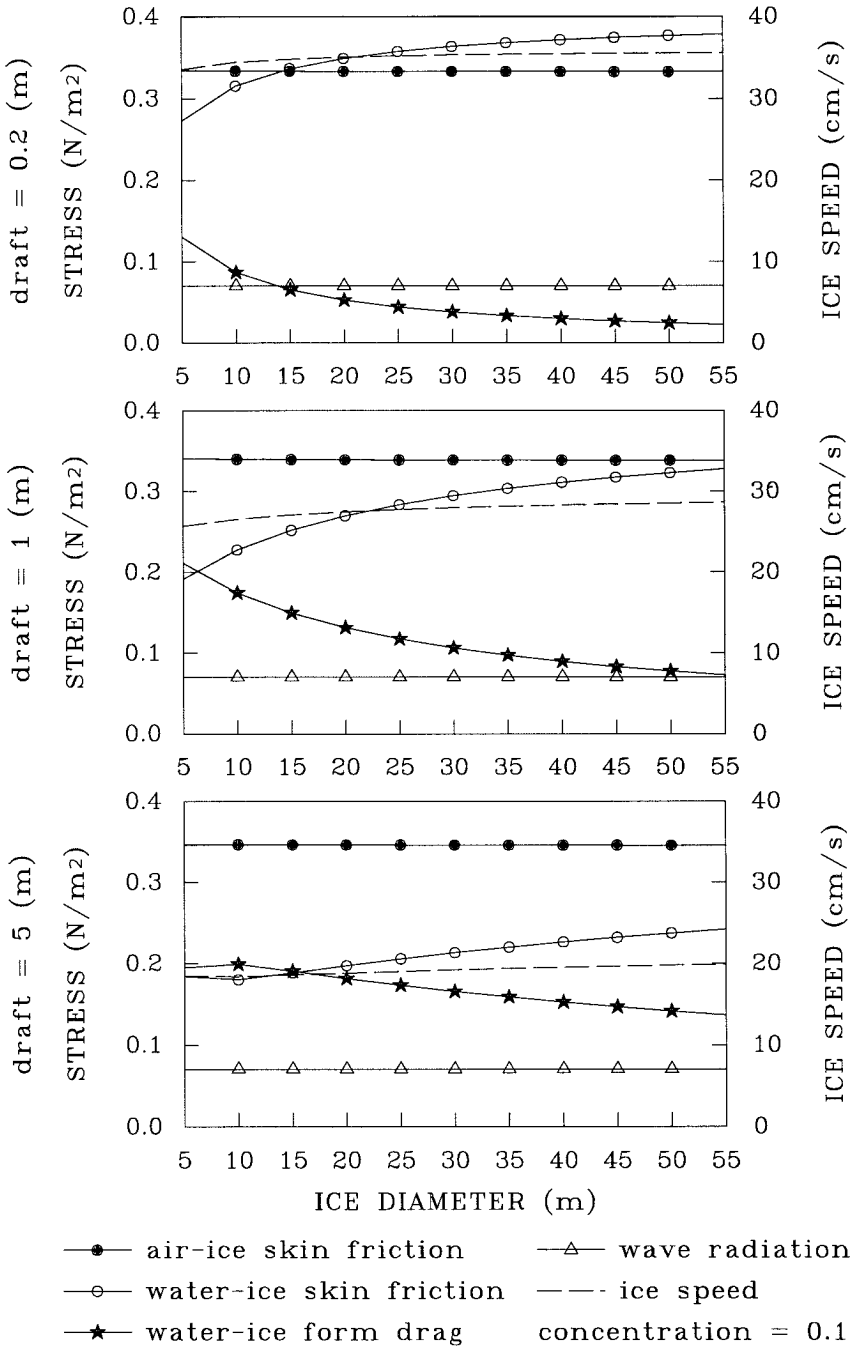

FIG. 4 (*Continued*). (d) Ice floe stresses and ice floe velocity for 10% ice cover concentration, ice drafts of 0.2, 1, and 5 m, as a function of ice floe diameter.

convergence/divergence occurs, (iii) these specific floes will largely remain *at the edge* of the ice floe field, and (iv) therefore these specific floes will remain part of, or in close proximity to, the 10% contour.

We neglect the geostrophic velocity $\mathbf{U}_g$ compared to the *absolute* ice floe velocity $\mathbf{u}'$ in Eq. (10). Thus we approximate the absolute ice floe velocity $\mathbf{u}'$ by the *relative* ice floe velocity $\mathbf{u} \equiv \mathbf{u}' - \mathbf{U}_g$. The plausibility for this approximation is given by Greenberg and Petrie (1988). They showed that the maximum barotropic circulation over the Newfoundland Shelf is $\sim$0.06 m s^{-1}. Although they estimated a somewhat higher maximum ($\sim$0.2 m s^{-1}) barotropic current over the Newfoundland slope, the ice edge contours of Fig. 8 are within the

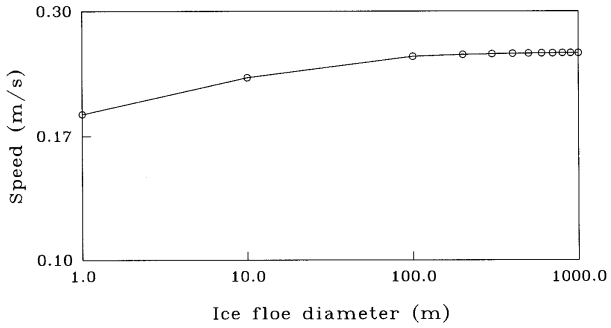

FIG. 5a. Mean ice floe speed as a function of floe diameter. These are estimated for young waves (wave age $0.77 < C_p/U_{10} < 0.97$). Wind speed U_{10} is 10 m s^{-1}. The scale is $\log_{10}$–$\log_{10}$. This shows that larger floes move faster. Concentration is 50% and floe draft is 2 m.

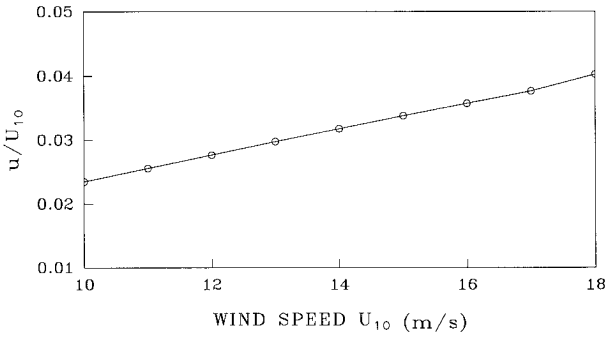

FIG. 5c. The ratio of mean ice floe speed to wind speed $\mathbf{u}/U_{10}$ as a function of U_{10} for young waves. Concentration is 50%, floe diameter and draft are 10 and 2 m.

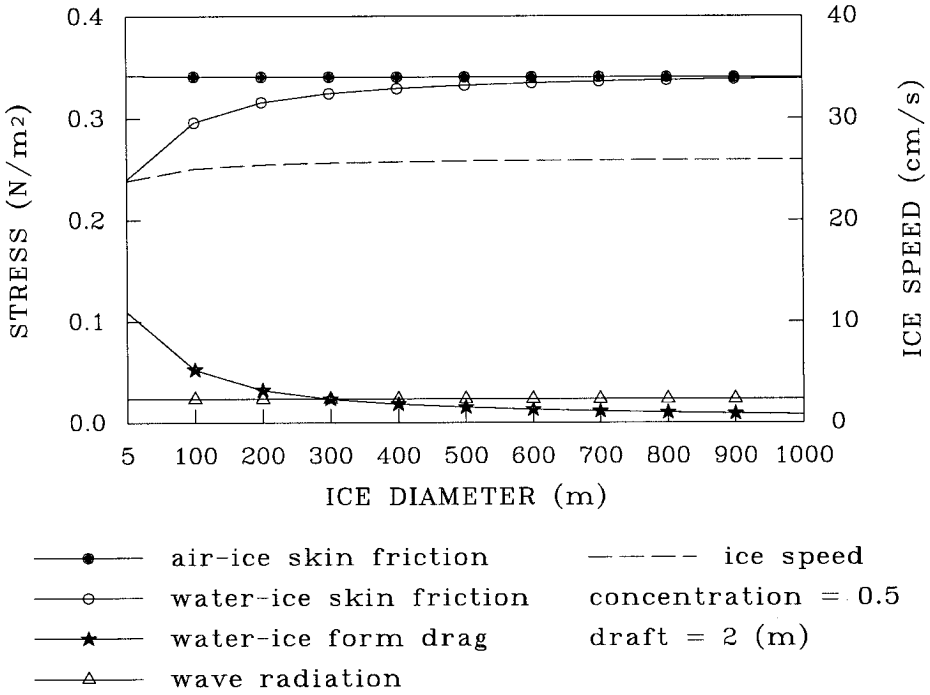

FIG. 5b. Ice floe stresses and ice floe velocity for 50% concentration and 2-m ice draft for floe diameters from 5 to 1000 m.

Newfoundland slope region. For the drift model, we have shown in Fig. 5c that the mean relative floe speed **u** varies from ~2.3% of U_{10}, when U_{10} = 10 m s^{-1}, to ~4% of U_{10} when U_{10} = 18 m s^{-1}. Thus, for the peak of the storm in Figs. 7a–b, when the modeled wind briefly reached 20 m s^{-1} at gridpoint positions other than the *Tydeman* or *Quest*, the wind-forced surface current is at least ~0.8 m s^{-1}. This is much larger than the corresponding geostrophic current $\mathbf{U}_g$. A related study is in preparation and will consider the contribution of the geostrophic current.

Figures 9a–b present the ice edge position on 15 and 18 March as estimated from the drift model. The observed ice edge is included for comparison. Model estimates were achieved by using bilinear interpolation to trace the trajectories of ice floes forming the initial ice edge elements. A *warm* start was used in the simulation, starting the *wave* component of the model on 9 March. By 11 March, the model sea state approximated the observed wave spectrum. The observed ice edge for 11 March was taken as the initial model ice edge for the ice edge forecasts for 15 and 18 March.

Ice thickness was assumed to be uniformly 0.8 m thick throughout the region inside the ice edge in Fig.

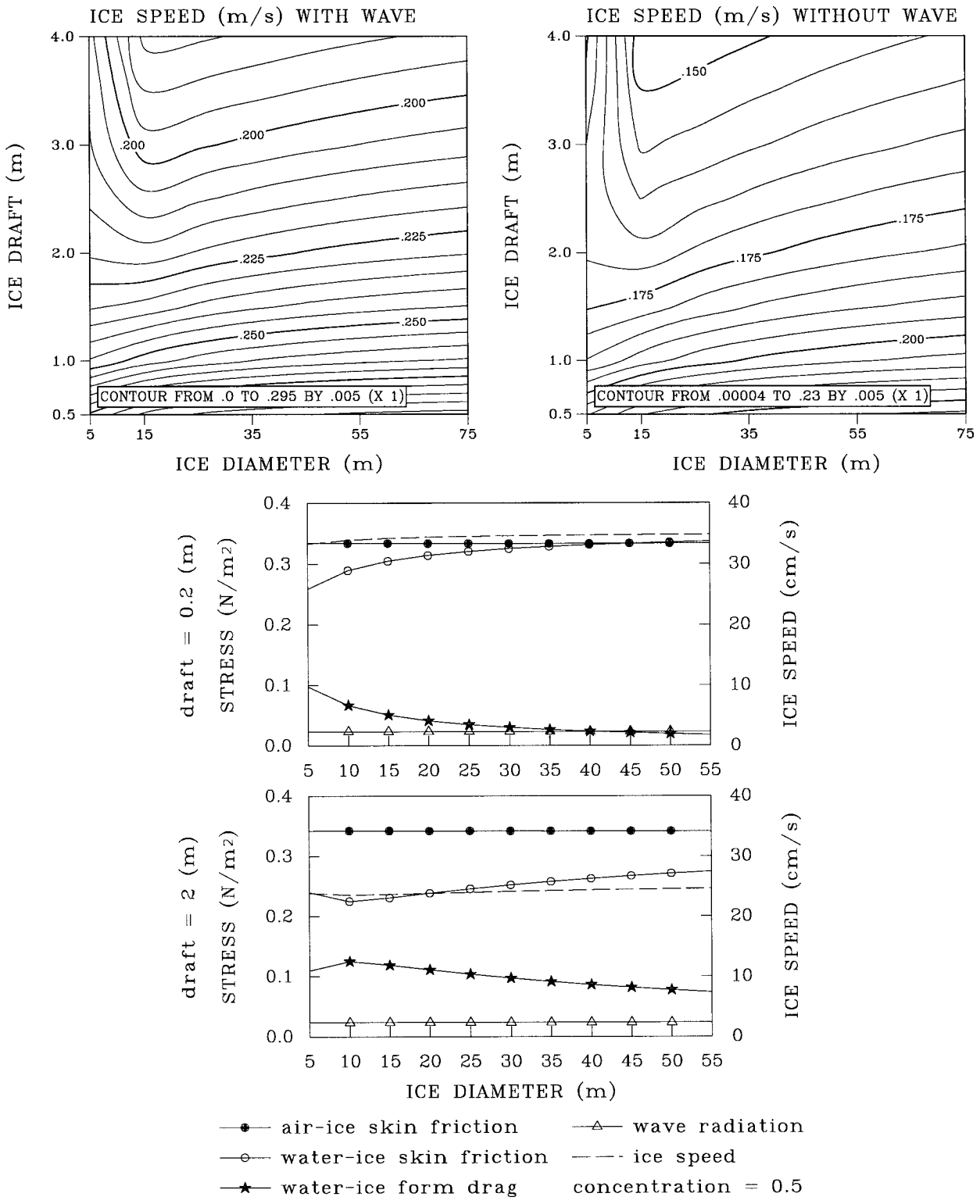

FIG. 6. (a: top) Ice floe speed (m s^{-1}) for 50% concentration and wind speed 10 m s^{-1} as a function of ice floe draft and diameter. Both wave and no-wave cases are presented. (b: bottom) Ice floe stresses and ice floe velocity for 50% concentration and ice drafts 0.2 and 2 m, as in (a) but for floe diameters from 5-m to 55-m.

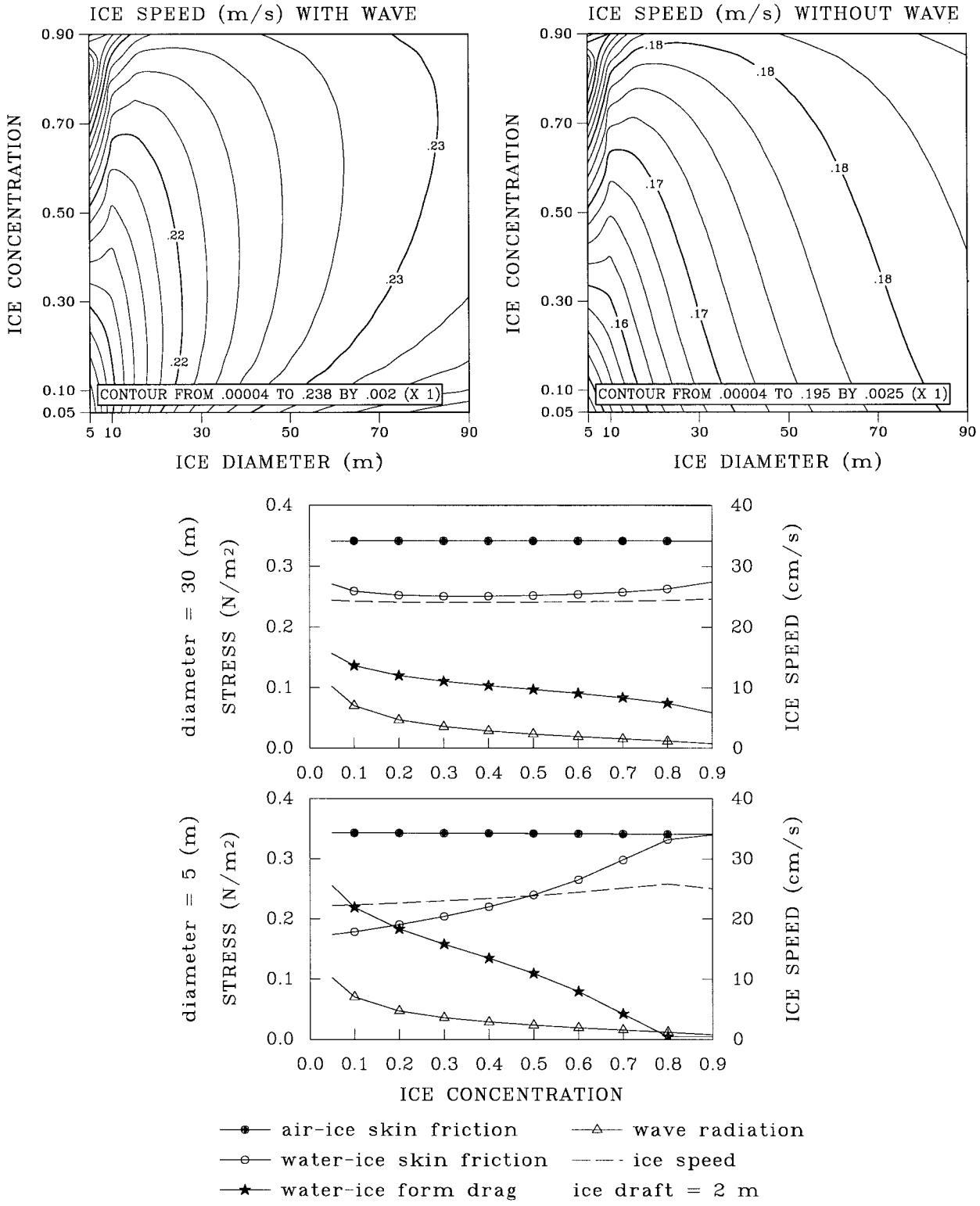

FIG. 6. (*Continued*). (c: top) Ice floe speed (m s^{-1}) for ice draft 2 m and wind speed 10 m s^{-1} as a function of concentration and diameter, as in (a). (d: bottom) Ice floe stresses and velocity for floe drafts 2 m and diameters 5 and 30 m, as in (c), as a function of concentration.

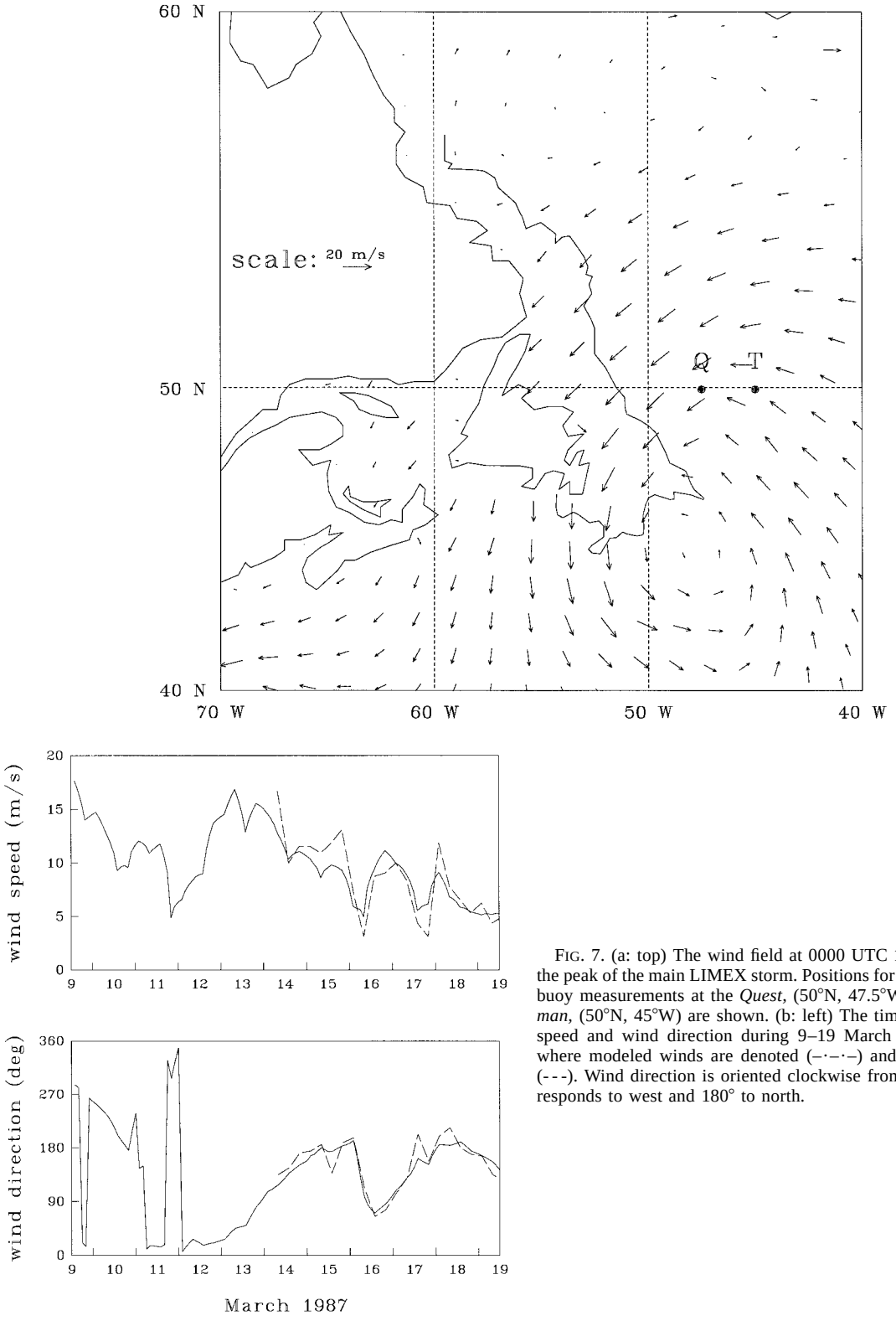

FIG. 7. (a: top) The wind field at 0000 UTC 14 March during the peak of the main LIMEX storm. Positions for directional wave buoy measurements at the *Quest*, (50°N, 47.5°W) and the *Tydeman*, (50°N, 45°W) are shown. (b: left) The time series of wind speed and wind direction during 9–19 March at the *Tydeman* where modeled winds are denoted (–·–·–) and observed winds (- - -). Wind direction is oriented clockwise from south: 90° corresponds to west and 180° to north.

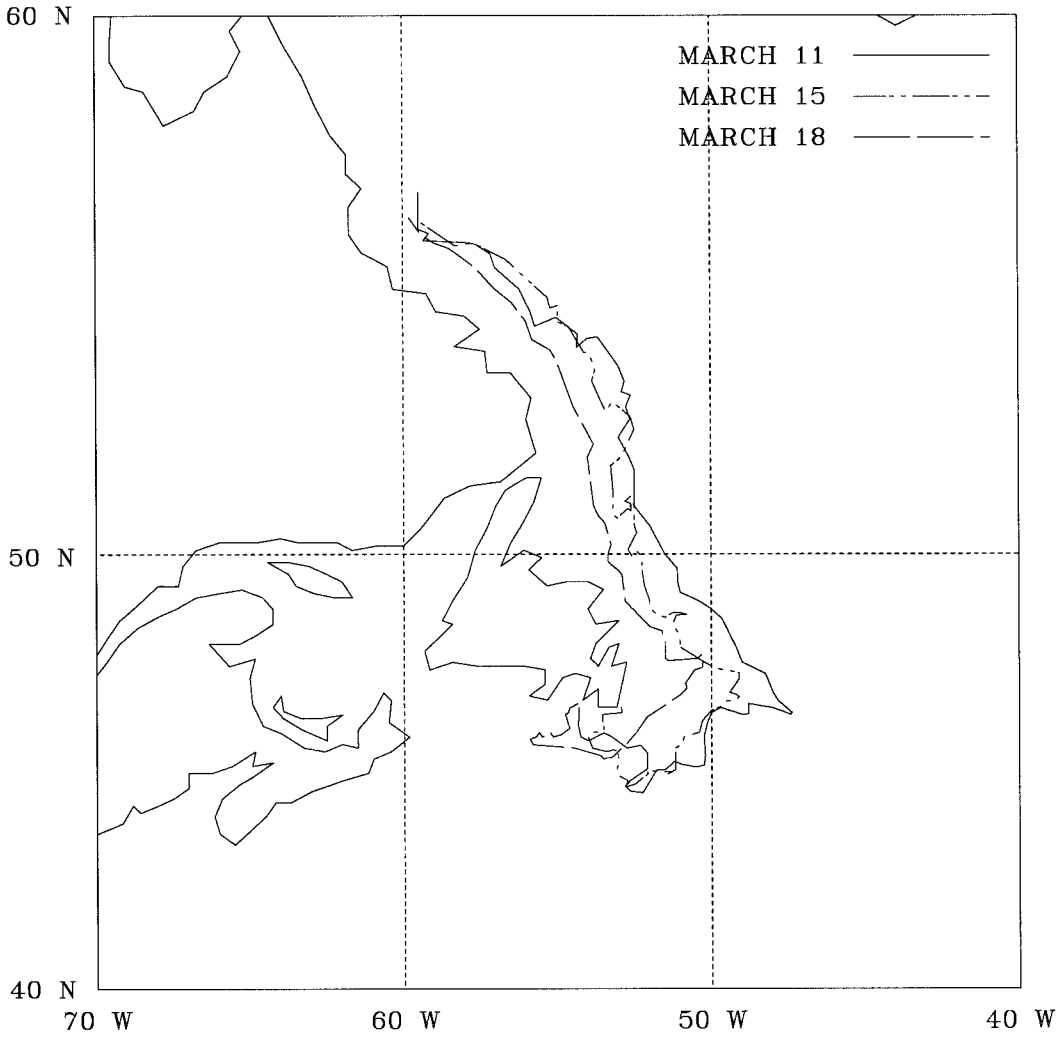

FIG. 8. The ice edge, as observed on 11, 15, and 18 March taken as the 10% ice cover concentration contour within the MIZ.

8. This is a *practical* approximation, because although first-year MIX ice is about 0.3–0.7 m thick, much of the interior ice field is about 0.7–1.20 m thick. Moreover, detailed ice thickness measurements are not available (S. J. Prinsenberg 1996, personal communication). The error in ice thickness contours from ice charts for the Grand Banks is on the scale of 100 km or greater. Ice floe diameters were assumed to be 20 m. Assumed values for the water–ice form drag coefficient C_{wi}^{f}, the water–ice skin friction drag coefficient C_{wi}^{s}, and the air–ice skin friction drag coefficient C_{ai}^{s} are 1.0, 0.03, and 0.002, respectively.

In estimating the position of the ice edge in Figs. 9a–b, we assume that while waves do travel into the ice field, the transmission of energy does not occur through the ice field, within either the wave or current fields. This is justifiable because, in almost all observations of large-scale ice floe fields on the Grand Banks of Newfoundland, the extent of the ice field is large enough that essentially no energy is transmitted from distant storms on the other side of the ice field. Part I of this study showed that swell energy would be dissipated by the time it reached the far edge of the ice sheet, except possibly very low frequency swell propagating from the southwest to northeast over the Grand Banks in the southern part of the ice field. Therefore, waves and wave-induced currents are assumed present at the ice edge only if the winds have a component that is on ice.

The agreement between the observed and modeled ice edge is relatively good on 15 March. This is hardly surprising because the highest wind speeds occurred during this period. Maximum winds reached 16.9 m s^{-1} on 13 March at the *Tydeman* and as much as 20 m s^{-1} at neighboring grid points. Thus, the winds were strong enough so that the wave model was able to reliably estimate the wave spectra. In contrast, the distinctive characteristic of 16–18 March is low wind speed. A minimum wind speed of 4.9 m s^{-1} was estimated on 16

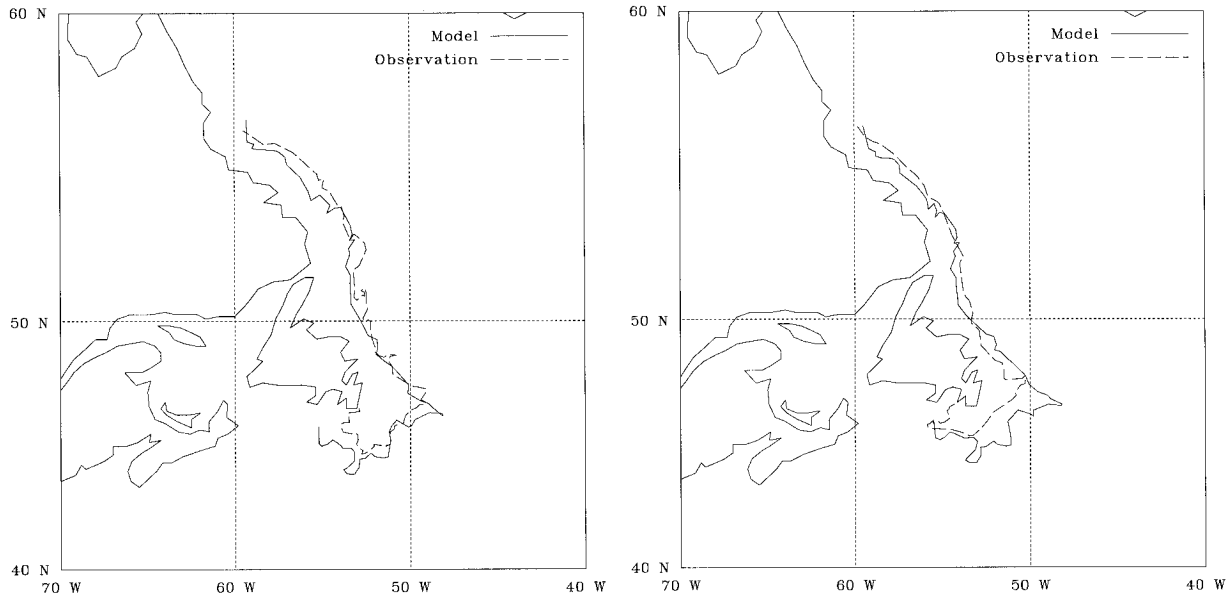

FIG. 9. Comparison of modeled and observed ice edges, assuming the ice floe thickness is 0.8 m, the air–ice skin friction drag coefficient C^s_{ai} is 0.002, and the water–ice skin friction drag coefficient C^s_{wi} is 0.03, respectively, (a) on 15 March and (b) on 18 March.

March at the *Tydeman* and as low as ~2 m s^{-1} at neighboring grid points. Figure 9b shows that resultant drift model estimates for the ice edge are also poor compared to observations. There are at least two possible explanations for this result.

1) Low wind fields generate low energy wave fields, which were poorly modeled by all LEWEX wave models in relation to measured wave spectra (Beal 1991).
2) Low wave fields, even if they could be modeled accurately, are less important compared to competing factors neglected by the drift model, for example, geostrophic currents.

To quantify the accuracy of the modeled ice edge, we define error ϵ in Figs. 9a–b as the difference between modeled and observed ice field areas, normalized by the observed ice field area, expressed as a percentage. Thus, summing over all subareas enclosed by modeled and observed ice edge contours $|c_i^{\text{observed}} - c_i^{\text{modeled}}|$,

$$\epsilon = \frac{\sum_{i=1}^{N} |c_i^{\text{observed}} - c_i^{\text{modeled}}|}{\text{total observed ice field}} \times 100 \qquad (19)$$

the modeled ice edge has an error ϵ of 27.4% on 15 March in Fig. 9a and 44.2% on 18 March in Fig. 9b. Corresponding ice edge estimates in the no-wave case result in similar errors of 26.5% and 43.0% for 15 and 18 March, respectively. To explore model sensitivity, assuming ice floe thickness of 1 m and water–ice and air–ice skin friction drag coefficients, C^s_{wi} and C^s_{ai}, of 0.02 and 0.003, the resultant errors are 29.4% and 45.2% for 15 and 18 March, respectively. Reducing the assumed ice floe thickness to 0.5 m results in errors of 33.0% and 48.4% for 15 and 18 March, respectively.

c. LIMEX—The wave field

Part I was concerned with wave attenuation due to ice floes, which were assumed not to drift. It was found that wave attenuation is *mostly* determined by ice cover concentration, wave frequency f, floe diameter, and wave age. Floe thickness, wind speed, wave energy $E(f, \vartheta)$, and MIZ floe position were found to be less important. In section 3 of this paper, we related ice floe drift to floe thickness, diameter, and ice cover concentration and showed the effect of waves. Sections 4a and 4b used the drift model to estimate the ice edge, neglecting the scattering–attenuation of waves by MIZ ice. However, ice drift and wave scattering–attenuation due to ice are different aspects of the same problem and should be considered together. In this section, we consider the drift of ice floes and the scattering–attenuation of waves, in a coupled scattering–drift model.

Implementing the scattering model of Part I into the *wave* component of the drift model, we estimate (i) the effect of MIZ wave scattering–attenuation on the ice edge, and (ii) the effect of ice floe drift on the wave spectra. Figure 10 presents the ice edge on 15 March as estimated from the combined scattering–drift model, assuming the same ice conditions and drag coefficients as used in Fig. 9a. However, in contrast to Figs. 9a–b we allow the scattering–attenuation component of the model to handle energy transmission through the ice field. We do not assume that transmission of energy does not occur *through* the ice field. The agreement between

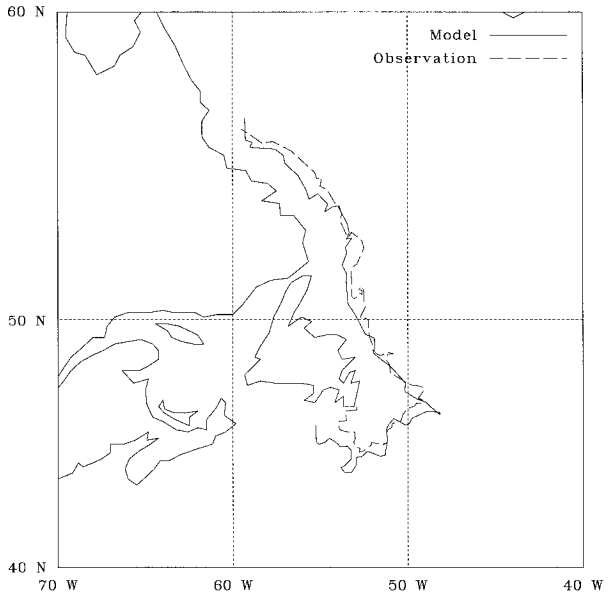

FIG. 10. Estimates for the ice edge on 15 March from the combined scattering–drift model, assuming the same ice floe parameters and drag coefficients C^s_{wi} and C^s_{ai} as in Figs. 9a–b.

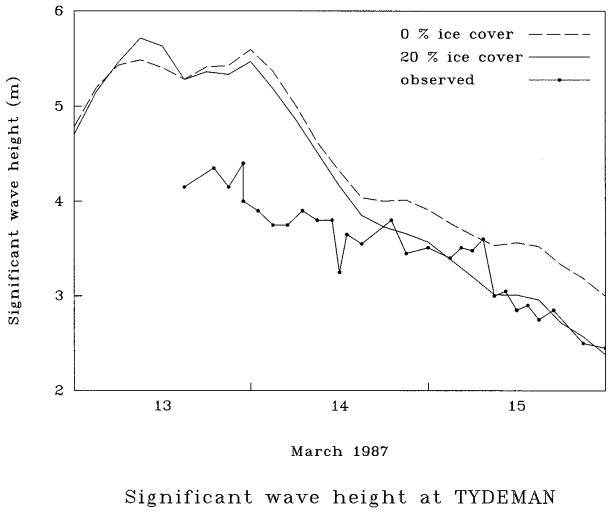

Significant wave height at TYDEMAN

FIG. 11. Time series of significant wave heights H_s at the *Tydeman* as measured by a directional buoy, in comparison with model estimates assuming ice floe diameters 10 m, thicknesses 1 m, and 0% and 20% ice cover. The rms deviation, $\sqrt{\sum_{j=1}^{N} (H_{s_{observed}} - H_{s_{modelled}})^2}$, is 503 assuming 0% ice cover, and 401 assuming 20% ice cover, as computed at 3-hourly intervals from 0300 UTC 13 March to 0000 UTC 16 March.

modeled and observed ice edges is comparable to that achieved in Fig. 9a, where no *scattering* mode was present in the model. The error between modeled and observed ice edges is 27.8% for 15 March in Fig. 10. For 18 March the error is 44.7%.

Figure 11 presents time series for measured significant wave heights H_s at the *Tydeman,* as given by Gerling (1991), in comparison with the scattering–drift model. The comparison is for the high wind period of 0300 UTC 13 March to 0000 UTC 16 March. We assume ice floe thickness 1 m, diameter 10 m, and ice cover concentrations fi, at 0% and 20%. Most of the dissipative effects (the reduction in wave heights) are achieved assuming fi = 20% and floe diameter 10 m, implemented on the large spatial scales covering the ice field. Further tests assuming 40%, . . . or higher concentrations, or floe diameters of 20 m, give similar results. Thus, assuming the presence of ice gives better agreement between modeled and observed H_s than assuming no ice. Moreover, neglecting the ice edge, a common feature of all LEWEX wave models, gives an overprediction of H_s during 13–15 March, although Beal (1991) suggests that this may also result from wind field errors near the peak of the storm.

The difference between the presence and absence of ice in wave spectra estimates is best shown at 0000 UTC 16 March. At this time, the wind speed is diminishing rapidly. The wind direction is from the south and slowly changing. The observed two-dimensional wave spectrum, as given in Fig. 12a from Gerling (1991), consists of a single peak at ~135°, with no swell. Model estimates for the wave spectrum are given in Fig. 12b, assuming 0% and 20% ice cover. In the *ice* case, the scattering–drift model suggests a single peak for the wave spectra, which at ~165° approximates the observed direction and peak magnitude of the wave spectral. In the *no ice* case, the scattering–drift model gives a peak wave direction also at ~165°, although the estimated wave peak magnitude is slightly too high. Moreover, the no-ice case exhibits an intense swell at ~315°, which is not observed. A similar swell energy is reported by Gerling (1991) in results obtained by the WAM wave model (Hasselmann et al. 1988), which also neglected ice.

Assuming ice is present gives wave spectra that more closely compare with observed spectra than when ice is assumed absent. However, this test is not a complete verification of the details of the model. Neglecting the *scattering* component of the model, and assuming no transmission of energy through the ice field, gives almost the same wave spectrum as the left panel of Fig. 12b. A test to verify details of the scattering component from the model would require high quality observations from a position much closer to MIZ floes than the *Quest* or *Tydeman.*

5. Conclusions

Steele et al. (1989) made important progress in trying to understand the balance of forces that impact on the motion of ice floes. Their formulations for air–ice and water–ice skin friction stress, $\boldsymbol{\tau}^{skin}_{air}$ and $\boldsymbol{\tau}^{skin}_{water}$, water–ice form stress $\boldsymbol{\tau}^{form}_{water}$, and wave radiation pressure $\boldsymbol{\tau}^{wave}_{rad}$ allowed estimation of ice floe speed as a function of a variety of parameters, such as floe thickness, diameter, and ice cover concentration. However, their approach

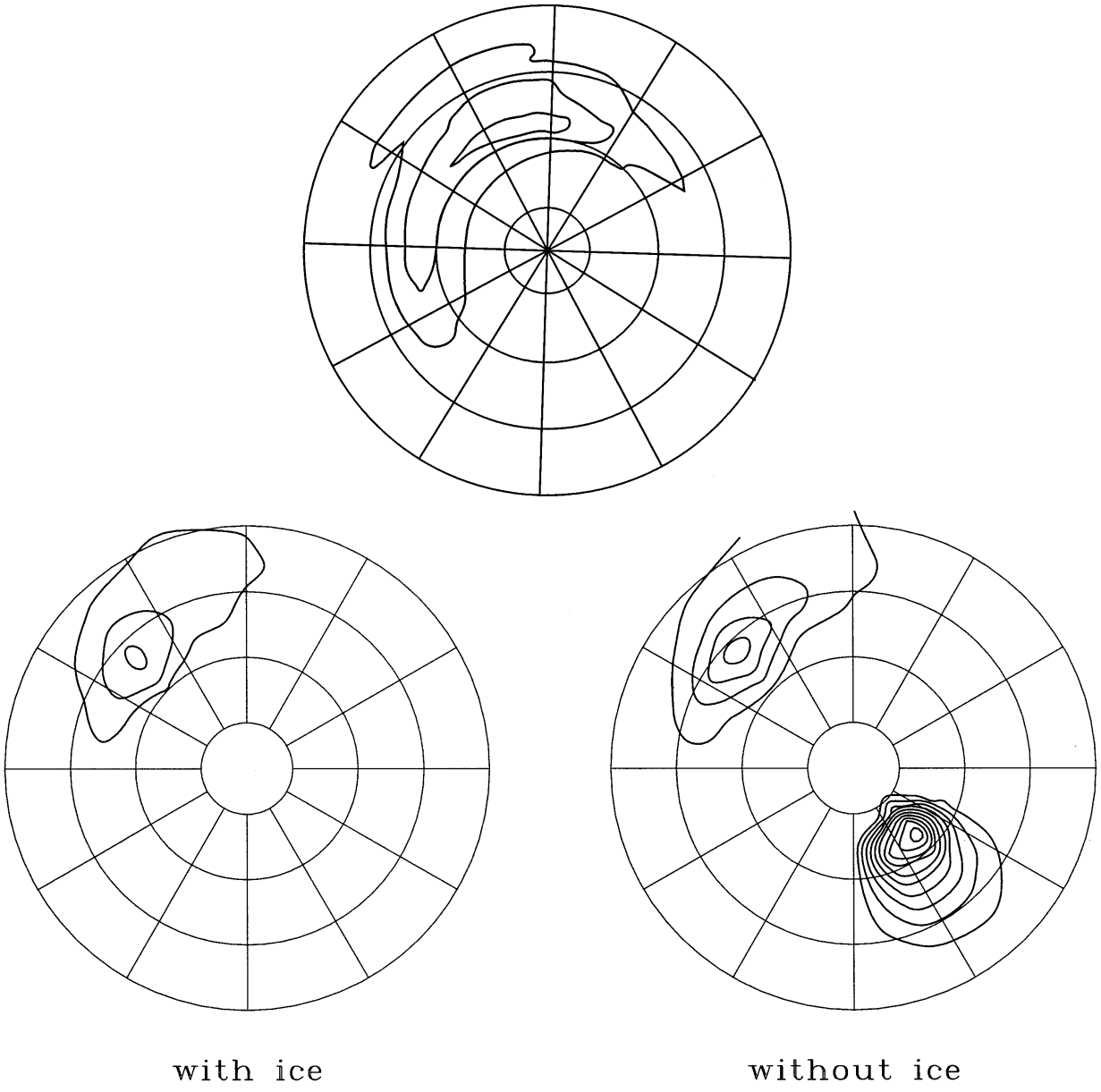

FIG. 12. The two-dimensional wave spectrum (a = top) at 0000 UTC 16 March as measured by the directional WAVESCAN buoy moored at the *Tydeman* and (b = bottom) corresponding model estimates. Ice floes are assumed to have 1-m thickness and 10-m diameter and ice cover is assumed (i) 0% and (ii) 20%.

cannot perform modeling of the ice edge with detailed consideration of wave-induced surface currents and wave scattering by ice floes. Using an operational spectral wave model with wave-induced currents following Jenkins (1987a,b), we have considered wind, wave, and current drag forces. Thus, we have inferred MIZ ice floe trajectories, as well as wave spectra in neighboring open ocean water.

We have shown that the presence of waves gives an enhancement to floe velocities and displacements, compared with assuming no waves. The difference is ~25% for either a constant or a time-varying wind field. The latter exhibits an enhanced floe speed partly because the drag coefficient for young waves may be as much as 3 times the drag coefficient for old waves (Smith et al. 1992). Moreover, waves confer a radiative wave pres-

sure $\tau_{\text{rad}}^{\text{wave}}$ on the stress balance for each ice floe, which can be important relative to air–ice skin stress $\tau_{\text{air}}^{\text{skin}}$, water–ice skin stress $\tau_{\text{water}}^{\text{skin}}$, and water–ice form stress $\tau_{\text{water}}^{\text{form}}$, especially for small thick ice floes in low concentration situations.

We showed that ice floe geometry and wind speed have impact on floe velocity. Thick floes move more slowly than thin floes. This is due to the decrease in surface currents with increasing depth, which is associated with an increase in $\tau_{\text{water}}^{\text{form}}$, despite a reduction in $\tau_{\text{water}}^{\text{skin}}$. For example, increasing the floe thickness from 0.2 to 0.8 m reduces the floe velocity by ~30%. Moreover, wide diameter floes move faster than small diameter floes. As floe diameter increases, $\tau_{\text{water}}^{\text{form}}$ decreases, which more than balances increases in $\tau_{\text{water}}^{\text{skin}}$. Whereas floes 1 m in diameter move at ~2% of the wind speed, floes 500 m in diameter move at ~2.5% of the wind speed. Furthermore, floe speed also increases monotonically with wind speed. We showed that floe speed varies from ~2.3% of U_{10} when $U_{10} = 10$ m s^{-1}, to ~4% of U_{10} when $U_{10} = 18$ m s^{-1}. This is influenced by the variation of surface current with increasing wind speed. Different assumptions about modeling the high-frequency wave spectrum within the wave model alter the surface current.

The wake effect suggested by Steele et al. (1989) for small diameter, thick floes, in high concentration fi situations, is evident in model estimates. Given small thick high-fi floes, then as fi increases, $\tau_{\text{water}}^{\text{form}}$ decreases, $\tau_{\text{water}}^{\text{skin}}$ increases, and floe speed increases, despite decreases in $\tau_{\text{rad}}^{\text{wave}}$. Conversely, low-fi corresponds to high $\tau_{\text{rad}}^{\text{wave}}$. Given small thick low-fi floes, then as fi increases, $\tau_{\text{water}}^{\text{form}}$ decreases rapidly, $\tau_{\text{water}}^{\text{skin}}$ increases, and floe speed also increases, despite decreasing $\tau_{\text{rad}}^{\text{wave}}$. Moreover, for moderate floes (~20–60 m), $\tau_{\text{water}}^{\text{skin}}$ is almost invariant with respect to fi. Therefore, as $\tau_{\text{water}}^{\text{form}}$ and $\tau_{\text{rad}}^{\text{wave}}$ approximately vary at the same rate, floe speed is largely fi-independent.

Estimates were made for ice edge evolution in response to forcing by winds, waves, and currents, modeling the MIZ ice edge as a collection of ice floes. It was demonstated that scattering–drift model estimates of ice edge evolution are largely comparable to LIMEX ice edge observations in high wind situations. During low LIMEX wind situations, wave estimates and ice edge predictions were poor. Moreover, during high wind situations, estimates for the two-dimensional wave spectra are more consistent with observed wave spectra when ice is assumed present than when it is neglected. Waves exert stress $\tau_{\text{rad}}^{\text{wave}}$ on the ice floes, which affects ice floe drift, which in turn cause scattering and attenuation of the waves, affecting the wave spectrum.

Unfortunately, LIMEX data was not able to provide a discriminating test of estimated ice drift and the wave spectra for the scattering–drift model, compared to merely the drift model. During LIMEX, estimates for wave spectra at the *Tydeman* from the scattering–drift model were often identical to estimates from the drift model. Estimates for ice edge evolution from the wave and no-wave cases were similar. In spite of this, we note that the physical mechanisms investigated were indeed shown to be important in *realistic* hypothetical situations. That they did not show themselves important in the rather low-wind conditions of the LIMEX dataset does not imply they cannot be important in severe storm situations. A discriminating test would require high-quality field data, collected for storm conditions. Data should be collected at positions close enough to MIZ floes for scattering attenuation of waves to be important in the observed wave spectra. Detailed observations of the MIZ ice floes and wind fields should also be made.

Acknowledgments. The wave modeling program at BIO is funded by the Federal Panel on Energy Research and Development (Canada) under Project No. 6B3006. The authors wish to acknowledge many important detailed and challenging comments from two anonymous reviewers.

REFERENCES

Beal, R. C., 1991: *Directional Ocean Wave Spectra: A Record of the Labrador Sea Extreme Waves Experiment.* The Johns Hopkins University Press, 218 pp.

Cardone, V. J., 1991: The LEWEX wind fields and baseline hindcast. *Proc. Symp. on Labrador Sea Extreme Waves Experiment,* Laurel, MD, The Johns Hopkins University Applied Physics Laboratory, 136–146.

Churchill, J. H., and G. T. Csanady, 1983: Near-surface measurements of quasi-Lagrangian velocities in open water. *J. Phys. Oceanogr.,* **13,** 1669–1679.

Gerling, T., 1991: A comparative anatomy of the LEWEX wave systems. *Proc. Symp. on Labrador Sea Extreme Waves Experiment,* Laurel, MD, The Johns Hopkins University Applied Physics Laboratory, 182–195.

Greenberg, D. A., and B. D. Petrie, 1988: The mean barotropic circulation on the Newfoundland shelf and slope. *J. Geophys. Res.,* **93**(C12) 15 541–15 550.

Hasselmann, K., T. P. Barnett, E. Bouws, H. Carlson, D. E. Cartwright, Enke, K., Ewing, J. A., Gicnapp, H., Hasselmann, D. E., Kruseman, P., Meerburg, A., Miller, P., Olbers, D. J., Richter, K., Sell, W., H. Walden, 1973: Measurements of wind-wave growth and swell decay during the Joint North Sea Wave Project (JONSWAP). *Dtsch. Hydrogr. Z.,* Erganzungsheft Reihe A (8), Nr. (12), 95 pp.

Hasselmann, S., K. Hasselmann, G. K. Komen, P. Janssen, J. A. Ewing, and V. Cardone, 1988: The WAM model—A third generation ocean wave prediction model. *J. Phys. Oceanogr.,* **18,** 1775–1810.

Hoerner, S. F., 1965: *Fluid-Dynamic Drag: Practical Information on Aerodynamic Drag and Hydrodynamic Resistance.* AIAA, 452 pp.

Huang, N. E., 1971: Derivation of Stokes drift for a deep-water random gravity wave field. *Deep-Sea Res.,* **18,** 255–259.

Jenkins, A. D., 1987a: Wind and wave induced currents in a rotating sea with depth varying eddy viscosity. *J. Phys. Oceanogr.,* **17,** 938–951.

——, 1987b: A Lagrangian model for wind- and wave-induced near-surface currents. *Coastal Eng.,* **11,** 513–526.

——, 1989: The use of a wave prediction model for driving a near-surface current model. *Dtsch. Hydrogr. Z.,* **42,** 134–149.

Madsen, O. S., 1977: A realistic model of the wind-induced Ekman boundary layer. *J. Phys. Oceanogr.,* **7,** 248–255.

McNutt, L., S. Argus, F. Carsey, B. Holt, J. Crawford, C. Tang, A. L. Gray, and C. Livingstone, 1988: LIMEX'87: The Labrador Ice Margin Experiment, March 1987—A pilot experiment in anticipation of RADARSAT and ERS-1 data. *Eos,* **69** (23), pp. 634–635, 643.

Perrie, W., and B. J. Toulany, 1985: Assessing a wave model à la SWAMP. Canadian Tech. Rep. of Hydro. and Ocean Sci. No. 67, 78 pp. [Available from Bedford Institute of Oceanography, P.O. Box 1006, Dartmouth, NS B2Y 4A2, Canada.]

——, and ——, 1990: Fetch relations for wind-generated waves as a function of wind-stress scaling. *J. Phys. Oceanogr.,* **20,** 1666–1681.

——, and Y. Hu, 1996: Air-ice-ocean momentum exchange. Part I: Energy transfer from waves to ice floes. *J. Phys. Oceanogr.,* **26,** 1705–1720.

——, H. Gunther, W. Rosenthal, and B. Toulany, 1989: Modelling wind-generated surface gravity waves using similarity in a coupled discrete wave model. *Quart. J. Roy. Meteor. Soc.,* **115,** 1373–1396.

Phillips, O. M., 1985: Spectral and statistical properties of the equilibrium range in wind-generated gravity waves. *J. Fluid Mech.,* **156,** 505–531.

Resio, D. T., 1981: The estimation of wind-wave generation in a discrete spectral model. *J. Phys. Oceanogr.,* **11,** 510–525.

Smith, S. D., 1988: Coefficients for sea surface wind stress, heat flux and wind profiles as a function of wind and temperature. *J. Geophys. Res.,* **93,** 15 467–15 472.

——, 1991: Some early results of the humidity exchange over the sea main experiment. *Deep Convection and Deep Water Formation in the Oceans,* P. C. Chu and J. C. Gascard, Eds., Elsevier Science, 377–382.

——, R. J. Anderson, W. A. Oost, C. Kraan, N. Maat, J. DeCosmo, K. B. Katsaros, K. L. Davidson, K. Bumke, L. Hasse, and H. M. Chadwick, 1992: Sea surface wind stress and drag coefficients: The HEXOS results. *Bound.-Layer Meteor.,* **60,** 109–142.

Steele, M., J. H. Morison, and N. Untersteiner, 1989: The partition of air-ice-ocean momentum exchange as a function of ice concentration, floe size, and draft. *J. Geophys. Res.,* **94,** 12 739–12 750.

The SWAMP Group, 1985: *Ocean Wave Modeling.* Plenum, 256 pp.

Tang, C., and D. Fissel, 1991: A simple ice–ocean coupled model for ice drift in marginal ice zones. *J. Mar. Syst.,* **2,** 465–475.

Thorpe, S. A., 1986: Measurements with an automatically recording inverted echo sounder: AIRES and the bubble clouds. *J. Phys. Oceanogr.,* **16,** 1462–1478.

——, 1992: Bubble clouds and the dynamics of the upper ocean. *Quart. J. Roy. Meteor. Soc.,* **118,** 1–22.

Toba, Y., and H. Kawamura, 1996: Wind-wave coupled downward-bursting boundary layer (DBBL) beneath the sea surface. *J. Oceanogr. Soc. Japan,* **52,** 409–419.

Wadhams, P., 1983: A mechanism for the formation of ice edge bands. *J. Geophys. Res.,* **88,** 2813–2818.

Weber, J., 1981: Ekman currents and mixing due to surface gravity waves. *J. Phys. Oceanogr.,* **11,** 1431–1435.

Yoshikawa, I., H. Kawamura, K. Okuda, and Y. Toba, 1988: Turbulent structure in water under laboratory wind waves. *J. Oceanogr. Soc. Japan,* **44,** 143–156.